



HAL
open science

Uranium mobility and deposition over 1.3 Ga in the Westmoreland area (McArthur Basin, Australia)

Joséphine Gigon, Julien Mercadier, Irvine Annesley, Antonin Richard, Andrew S. Wygralak, Roger G. Skirrow, Terrence Mernagh, Ion Probe Team Nancy

► **To cite this version:**

Joséphine Gigon, Julien Mercadier, Irvine Annesley, Antonin Richard, Andrew S. Wygralak, et al.. Uranium mobility and deposition over 1.3 Ga in the Westmoreland area (McArthur Basin, Australia). *Mineralium Deposita*, 2021, 56 (7), pp.1321-1344. 10.1007/s00126-020-01031-2 . hal-04772490

HAL Id: hal-04772490

<https://hal.science/hal-04772490v1>

Submitted on 13 Feb 2025

HAL is a multi-disciplinary open access archive for the deposit and dissemination of scientific research documents, whether they are published or not. The documents may come from teaching and research institutions in France or abroad, or from public or private research centers.

L'archive ouverte pluridisciplinaire **HAL**, est destinée au dépôt et à la diffusion de documents scientifiques de niveau recherche, publiés ou non, émanant des établissements d'enseignement et de recherche français ou étrangers, des laboratoires publics ou privés.



Distributed under a Creative Commons Attribution 4.0 International License

Uranium mobility and deposition over 1.3 Ga in the Westmoreland area (McArthur Basin, Australia)

Joséphine Gigon¹, Julien Mercadier¹, Irvine R. Annesley¹, Antonin Richard¹, Andrew S. Wygralak², Roger G. Skirrow³, Terrence P. Mernagh⁴, Ion Probe Team Nancy⁵

¹Université de Lorraine, CNRS, CREGU, GeoRessources, F-54500 Vandœuvre-lès-Nancy, France

²Northern Territory Geological Survey, PO Box 2901, Darwin, NT 0801, Australia

³Geoscience Australia, GPO Box 378, Canberra, ACT 2601, Australia

⁴Australian National University, 142 Mills Rd., Acton, ACT 2601, Australia

⁵CRPG, UMR 7358, CNRS, Université de Lorraine, Vandœuvre-lès-Nancy F-54501, France

Corresponding author: josephine.gigon@gmail.com; +33 3 72 74 55 59

JG: <https://orcid.org/0000-0001-5971-9659>

RS: <https://orcid.org/0000-0002-9684-1554>

TM: <https://orcid.org/0000-0002-8555-0110>

Abstract

The Westmoreland area is located south of the McArthur Basin (Australia) and hosts several uranium (U) deposits and prospects. Previous studies proposed that U mineralisation formed under conditions similar to the unconformity-related U deposits of the Alligator Rivers Uranium Field (ARUF), located north of the same sedimentary basin. Detailed mineralogical, geochemical and geochronological studies on mineralised intervals from the Redtree, Junnagunna and Huarabagoo deposits, and integration with previous studies, identified at least six generations of uranium oxides. These formed between ca. 1680 and 350 Ma, highlighting protracted mobility of U over 1.3 Ga. Each generation of uranium oxide has a specific chemical composition, indicating variable physico-chemical conditions for their formation throughout this period.

Although the 1680 Ma mineralising event formed at the same time and with similar mineralising fluids as the unconformity-related U deposits from the ARUF, the physico-chemical conditions differed between the two

26 areas. Deposits of the Westmoreland area lack the typical Mg- and B-metasomatism of the unconformity-related
27 U deposits in the ARUF: in the Westmoreland area, the chlorite is Mg-poor and no B minerals are observed,
28 whereas the ARUF is marked by Mg-rich chlorite (between the clinocllore and Mg-amesite fields), Mg-foitite
29 (tourmaline), and alumino-phosphate-sulphate minerals. The chondrite-normalized REE patterns of uranium
30 oxides are enriched in LREE or flat, compared with the typical bell-shape of the unconformity-related U
31 deposits. Moreover, chlorite thermometry indicates significantly higher temperature conditions (>300°C) than in
32 the ARUF for the early U stages. Based on these results, it is thus unlikely that the mineralisation in the
33 Westmoreland area can be linked to significant unconformity-related U deposits in this area. Collectively, the
34 data point towards atypical ore-forming processes for basin-related U deposits in the Westmoreland area
35 compared with known processes in the ARUF and in other sedimentary basins.

36 **Keywords**

37 Uranium, Australia, Westmoreland, U-Pb isotopic ages, uraninite REE patterns, chlorite thermometry

38 **1. Introduction**

39 The Westmoreland area (Northern Territory and Queensland, Australia) hosts several U deposits and prospects
40 located in the Paleo- to Mesoproterozoic McArthur Basin and related crystalline basement (Polito et al. 2005a;
41 Ahmad et al. 2013; International Atomic Energy Agency 2018a, Figs. 1 and 2). The area hosts five deposits
42 (Redtree, Junnagunna, Huarabogoo, Outcamp and Sue) that are classified as Westmoreland-Murphy-type U
43 deposits (Lally and Bajwah 2006), and have indicated combined resources for all the deposits totalling ~ 16 000 t
44 U contained within 18.7 million tonnes at an average grade of 0.089% U₃O₈, and an inferred mineral resource
45 totalling ~ 7 000 t U contained within 9.0 million tonnes at an average grade of 0.083% U₃O₈ (JORC and NI 43-
46 101 compliant resource, Laramide Resources Ltd 2019). These deposits and related occurrences are part of a set
47 of deposits known in this large intracratonic basin, with several mineralised areas concentrating various types of
48 metals (U, Pb, Zn, and Cu, Ahmad et al. 2013). U deposits are found in the Pine Creek Orogen (northern part of
49 the basin) and in the Westmoreland area (southern part), Cu-bearing breccia pipes and minor vein-type
50 mineralisation are present in the Redbank area in the southeastern part of the basin (e.g. Knutson et al. 1979),
51 and SHMS Zn-Pb deposit are mostly found in the centre of the basin (e.g. Gigon et al. 2020).

52 The geological processes and physico-chemical conditions for the origin of the different U deposits found in the
53 McArthur Basin have been studied for decades. The Alligator Rivers Uranium Field (ARUF) to the North hosts
54 the Jabiluka, Ranger, Nabarlek and Koongarra U deposits among others belonging to the unconformity-related
55 deposits type, for which the processes related to the U deposition have been studied extensively (e.g. Wilde and
56 Wall 1987; McKay and Miezeitis 2001; Derome et al. 2003; Polito et al. 2004, 2005b, 2011; Lally and Bajwah
57 2006; Fisher et al. 2013; Clauer et al. 2015; Skirrow et al. 2016; Gigon et al. 2019). U deposits from the
58 Westmoreland area have comparatively attracted much less attention (Hills and Richards 1976; Fuchs and
59 Schindlmayer 1981; Ahmad and Wygralak 1989 and references herein; Rheinberger et al. 1998; Polito et al.
60 2005a; Mernagh and Wygralak 2011), and the previous research (e.g. Polito et al., 2005a and Mernagh and
61 Wygralak 2011) mainly examined if these U deposits and related occurrences could be analogues to the
62 unconformity-related U deposits known at the border of the Northern part of the McArthur Basin, but also in the
63 Athabasca and Thelon basins (Canada; Jefferson et al. 2007; Cuney and Kyser 2015; Grare et al. 2020).
64 Unambiguously establishing such relationships with unconformity-related U deposits is indeed important
65 because unconformity-related U deposits have the highest grades and tonnages among all the U deposits, and are
66 therefore dominant U exploration target worldwide.

67 The results from the previous studies in the Westmoreland area indicate that the mineralogy, paragenesis and
68 geochemistry of the Redtree, Junnagunna and Huarabagoo deposits share some characteristics with the U
69 deposits of the ARUF (Polito et al. 2005a), thus suggesting that the timing and geological processes for the
70 origin of both U provinces were similar. The fluid inclusions in the Eva Mine and Jackson Pit U deposits,
71 yielded NaCl-rich and CaCl₂-rich brines and a low-salinity fluid that mixed in varying degrees (Mernagh and
72 Wygralak 2011), as also documented for the unconformity-related U deposits from the ARUF (Ypma and
73 Fuzikawa 1980; Durak et al. 1983; Derome et al. 2003, 2007; Polito et al. 2004, 2005b). These combined results
74 seem to indicate that the first-order parameters and the timing for the formation of both uranium provinces in the
75 McArthur Basin are identical. The main goal of the present work is thus to refine this comparison between the U
76 deposits of the ARUF and the Westmoreland area by verifying the possible metallogenetic relationships between
77 these two deposit subtypes.

78 New geochemical criteria applicable to uranium oxides, based on rare earth element content in uranium oxides,
79 allow classification of the different types of U deposits (Mercadier et al. 2011b; Frimmel et al. 2014; Alexandre
80 et al. 2016). Such criteria have been applied to the U deposits from the ARUF, confirming their affinity with the
81 U deposits from the Athabasca Basin (Canada) and thus their classification as unconformity-related U deposits

82 (Mercadier et al. 2011b). Application of such geochemical markers is lacking for the U deposits of the
83 Westmoreland area and this forms the first objective of this study. The second objective is to add to the existing
84 data on ore mineralogy, geochemistry and age dating for different mineralised intercepts of three U deposits
85 from Westmorland area: Redtree, Junnagunna and Huarabagoo. The final objective of this approach is to provide
86 new geochronological constraints on formation of the U deposits and occurrences of the Westmoreland area, in
87 particular the characterisation of potential multiple fluid events that favoured U mobility through time and space.
88 These new results are compared to previously published models for the area, to the unconformity-related
89 deposits of the ARUF, and to U deposits in other Proterozoic basins.

90 2. Geological settings

91 The Westmoreland area is adjacent to the Queensland-Northern Territory border on the south-eastern margin of the southern
92 McArthur Basin (Fig. 1). The oldest rocks in the Westmoreland region are Paleoproterozoic metasedimentary, volcanic and
93 felsic rocks from the Murphy Province that forms the basement to the McArthur Basin. The units in the Murphy Province are
94 the Murphy Metamorphics and a suite of comagmatic felsic intrusive and volcanic rocks known as the Nicholson Granite and
95 the Cliffdale Volcanics. The Murphy Metamorphics are essentially a succession of greenschist-facies metamorphosed shales
96 and greywackes (Ahmad et al. 2013). Uranium–lead data on detrital zircon suggest a maximum depositional age of 1853 ± 4
97 Ma (Hollis et al. 2010, Table SM1) and the sediments were metamorphosed prior to the extrusion of the Cliffdale Volcanics
98 (Ahmad et al. 2013). The Nicholson Granite Complex (Fig. 2) is intrusive in the Murphy Metamorphics and can be divided
99 into two broad suites based on chemical and mineralogical composition, one hornblende- and/or biotite bearing granite,
100 quartz monzonite and granodiorite and one biotite- and/or muscovite bearing monzonite, granite and alkali granite. Two
101 samples of the Nicholson Granite Complex have yielded SHRIMP U-Pb zircon ages of 1856 ± 3 and 1845 ± 3 Ma (Page et al.
102 2000, Table SM1). The Cliffdale Volcanics are a succession of more than 4km of rhyolite, dacitic lavas, ignimbrites and
103 intrusions that unconformably overlie the Murphy Metamorphics (Ahmad et al. 2013). SHRIMP U-Pb dating of zircons has
104 yielded an age of 1851 ± 3 Ma (Page et al. 2000 , Table SM1).

105 The Paleo–Mesoproterozoic McArthur Basin is an up to 10 km thick sequence of mostly unmetamorphosed
106 sedimentary and volcanic rocks deposited between 1815 and 1492 Ma that unconformably overlies the Murphy
107 Province (Ahmad et al. 2013). The basal unit of the McArthur Basin, the Westmoreland Conglomerate (Fig. 2),
108 is composed mainly of fluvial sandstones and conglomerates and is up to 1,800 m thick. It has been subdivided
109 into five stratigraphic units, each unit representing a major fining-upward cycle of sedimentation (Ahmad and
110 Wygralak 1989). Each unit comprises proximal fluvial deposits typical of debris flows, alluvial fans, and braided
111 river systems overlain by medium- to coarse-grained, well-sorted sandstones. Angular unconformities or

112 disconformities define breaks in sedimentation, with each new cycle of pebble or boulder conglomerate
113 commonly defining the beginning of a new unit. Cobbles and coarse sand grains within the basal conglomerate
114 are dominated by reworked quartz veins, chert, and clasts of felsic to mafic volcanic rocks that were likely
115 derived from basement rocks such as the Murphy tectonic ridge or similar rocks that once existed to the North
116 (Wygralak et al. 1988; Ahmad and Wygralak 1989; Polito et al. 2005a). The detrital lithic clasts, monazite,
117 zircon, and apatite are likely to be among the source of uranium that was dissolved during peak diagenesis
118 (Polito et al. 2005a and references herein). Most of the uranium mineralisation is hosted within the upper unit of
119 the Westmoreland Conglomerate (Ptw4), which is a 80–90 m thick porous, coarse-grained sandstone,
120 conglomeratic in part (International Atomic Energy Agency 2018a). U-Pb dating of detrital zircon from the
121 Westmoreland Conglomerate has returned maximum depositional ages of 1865 ± 7 Ma for the lower section and
122 1843 ± 4 Ma for the upper section (Ahmad and Wygralak 1990, Table SM1). The Westmoreland Conglomerate
123 is conformably overlain by the mafic Seigal Volcanics (basaltic lavas), followed by dolomite, sandstone, mafic
124 and felsic volcanic rocks of the upper part of the Tawallah Group. The deposition age of the Seigal Volcanics is
125 estimated at ca. 1780 Ma by stratigraphic correlation (Scott et al. 2000; Mernagh and Wygralak 2011).

126 Dolerite dykes and minor sills, which may have been feeders of the lava flows, intrude along North-Est trending
127 fault and fracture zones that intersect the Westmoreland Conglomerate (International Atomic Energy Agency
128 2018b). Uranium mineralisation is associated with three major northeast-trending lineaments (NE
129 Westmoreland, Redtree and El Nashfa dyke zones, Fig. 1), with the Redtree dyke zone extending over a strike of
130 20 km (Ahmad et al. 2013). The dykes has not been dated but they could have the same age as the Seigal
131 Volcanics (Ahmad and Wygralak 1989).

132 The Westmoreland region was first prospected in the 1890s for Pb-Zn, then for Cu, and finally U was mined
133 from the Peters Creek Volcanics which overlie the Westmoreland Conglomerate, 20 to 30 km west of Redtree
134 (Laramide Resources Ltd 2016). The Redtree, Junnagunna and Huarabagoo U deposits are hosted largely within
135 the shallow dipping Westmoreland Conglomerate near the unconformity with the Murphy Inlier and lie along the
136 Redtree dyke zone (Fig. 1). The U-rich zones can be oriented parallel to the volcanic rocks or sills, discordant at
137 the contact with mafic dykes, within fractures cross-cutting altered mafic volcanic rocks within fractures or
138 along shear zones in altered felsic volcanic rocks. The studied deposits belong to “mafic dykes/sills in
139 Proterozoic sandstone type” (International Atomic Energy Agency 2018b) or “Westmoreland-Murphy-type”
140 (Lally and Bajwah 2006). The deposits of the “mafic dykes/sills in Proterozoic sandstone” category are situated
141 in the Westmoreland area and within the Otish Basin (Canada). “Westmoreland-Murphy-type” deposits occur

142 within conglomerate, sandstone and mafic volcanic rocks, and are all associated with redox boundaries near the
143 contacts between different lithologies. In addition, in the studied region, uranium occurrences were classified by
144 Ahmad (1987) into five types (A–E), based on their hydrological and geological settings. Four of them are
145 present in the basin, and reported on Fig. 1. Type A deposits lie at the contact between the Westmoreland
146 Conglomerate and the Cliffdale or Seigal Volcanics (in sub-type A1 occurrences, the contact between the
147 Cliffdale Volcanics and Westmoreland Conglomerate is a reverse fault; in sub-type A2 deposits, the contact
148 between the Westmoreland Conglomerate and Seigal Volcanics is conformable). In type B deposits,
149 mineralisation occurs as sub-horizontal and sub-vertical lenses in the Westmoreland Conglomerate. Type C
150 deposits are hosted by intensely altered Cliffdale Volcanics; Type D occurrences are related to fractures in the
151 lower part of the Seigal Volcanics.

152 The bulk of the Westmoreland resource base (~50%) is located in the Redtree deposit. It flanks the Redtree dyke
153 zone immediately north of the northwest-trending Namalangi fault (Fig. 1). The Redtree dyke (20–30 m wide)
154 broadly extends for 7 km from Redtree to Junnagunna and spatially controls the distribution of U, indicating that
155 mineralizing fluids used this structure as a main drain uranium mineralising fluids probably used this structure
156 (Laramide Resources Ltd 2019). The deposit is characterised by a mix of horizontal and vertical lenses of
157 continuous mineralisation in distinctly coarse pebble conglomerates with grades ranging from 0.15% to >2%
158 U₃O₈ (Fig. 2). Mineralisation is generally shallow, within 10m of surface and is associated with chlorite/hematite
159 alteration. The mineralisation thickens and steepens near the dyke, where it is 30–40 m thick (International
160 Atomic Energy Agency 2018a). The indicated resource is 12.86 Mt of ore at an average grade of 0.09% U₃O₈
161 and an inferred resource of 4.47 Mt at an average grade of 0.07% U₃O₈ (JORC and NI 43-101 compliant,
162 Laramide Resources Ltd 2016).

163 The Junnagunna U deposit occurs at a fault intersection west of the Redtree dyke zone and south of the
164 northwest trending Cliffdale fault (Fig. 1). Mineralisation is generally flat lying on both sides of the Redtree
165 dyke and ranges from 0.5 m to 20 m in thickness beneath the Seigal-Westmoreland contact (Fig. 2). The deposit
166 is covered by alluvium/colluvium clays, sand and weathered Seigal Volcanics (Laramide Resources Ltd 2019).
167 The indicated resource is 4.36 Mt ore at an average grade of 0.08% U₃O₈ and an inferred resource of 2.15 Mt at
168 an average grade of 0.8% U₃O₈ (Laramide Resources Ltd 2016).

169 The Huarabagoo deposit is about 3 km NE of Redtree along the Redtree dyke zone and straddles the contact of
170 the Seigal Volcanics with the Westmoreland Conglomerate (Figs. 1 and 2). Mineralisation occurs in 20 m thick

171 lenses, which extend to 100–200 m length and to a depth of 80 m (Laramide Resources Ltd 2019). It outcrops at
172 the southern end and is concealed to the north under 2 to 3 m of sandy alluvium and 5 to 8 m of weathered basalt
173 of the Seigal Volcanics (Laramide Resources Ltd 2016). The deposit comprises a 3 km zone of vertical
174 mineralisation associated with a complex dyke geometry with vertical and horizontal branches between the two
175 principal dykes. The strongest mineralisation is associated with chlorite/hematite-altered coarse pebbly
176 sandstones similar to Redtree. Most of the mineralisation is hosted within the Westmoreland Conglomerate
177 adjacent to the dykes, and the remainder is hosted in the dykes (International Atomic Energy Agency 2018b).
178 Indicated resources are 1.46 Mt ore at an average grade of 0.08% U_3O_8 and inferred resources are 2.41 Mt at an
179 average grade of 0.11% U_3O_8 (Laramide Resources Ltd 2016).

180 **3. Sampling and methodology**

181 A multi-method approach was conducted on different minerals (uranium oxides, chlorite and apatite), from the
182 Junnagunna, Redtree and Huarabagoo deposits. A specific focus was the selection of samples within the highest-
183 grade parts of mineralised zones of the deposits, all located within the Westmoreland Conglomerate (Fig. 2).
184 This selection was also based on the paragenesis for the U deposits of the Westmoreland area established by
185 Polito et al. (2005a).

186 Five drill holes were sampled in three deposits based on their high U grade, representative of the different
187 mineralisation styles: JDD08-003 (Junnagunna), WDD9-128 (Huarabagoo), WDD10-151 (Huarabagoo),
188 WDD07-2 (Redtree), and WDD08-106 (Redtree). Mineralised intersections are: at Junnagunna, 0.21% U_3O_8 in
189 JDD08-003 from 71 to 76m; at Huarabagoo, 0.16% U_3O_8 in WDD10-151 between 22 and 31m; at Redtree,
190 0.25% U_3O_8 in WDD07-02 from 48 to 59m and 0.2% from 70 to 75m and 0.31% in WDD08-106 from 8 to 16m
191 (Vigar and Jones 2009; Laramide Resources Ltd 2016). The following samples were studied: JDD08-003 at
192 74.4m, WDD07-2 at 51.7, 55.9 and 73.5m, WDD9-128 at 53.3 and 92.3m, WDD10-151 at 29.4m and WDD08-
193 106 at 10.6m.

194 Selected thin sections were studied by optical and scanning electron microscope (SEM) to develop detailed
195 paragenetic sequences. The chemical composition for the major elements of chlorite and uranium oxide was
196 determined by Electron Probe Micro Analyses (EPMA). The isotopic U-Pb and Pb/Pb ages of uranium oxide and
197 apatite were determined by Secondary Ion Mass Spectrometry (SIMS). The concentrations of minor and trace

198 elements in uranium oxides were determined by Laser Ablation-Inductively Coupled Plasma-Mass Spectrometer
199 (LA-ICP-MS). The locations of the analyses are presented in Figs. SM1–SM8.

200 3.1. Petrography

201 Optical microscopy was carried out on thin sections using a numerical microscope VHX-200F with a high
202 resolution objective VH-Z500W to cover the whole sections and a Zeiss Axio Scope A1 microscope for detailed
203 petrography (GeoRessources Lab - Vandœuvre-lès-Nancy, France). SEM images and spectra were obtained
204 using BackScattered Electron detector (BSE) Tescan Vega3LM with a conventional tungsten source at SCMEM
205 (GeoRessources Lab - Vandœuvre-lès-Nancy, France). The analytical conditions were an acceleration voltage of
206 15 kV and beam current of around 0.1–1 nA.

207 3.2. Major elements composition of uraninite and chlorite

208 The quantitative measurements of major elements in uraninite and related chlorite were performed using a
209 CAMECA SX-100 Electron Probe MicroAnalyser (EPMA) at SCMEM with a spot size of $1\mu\text{m}^2$. For uraninite,
210 the calibration was based on natural and synthetic oxides and/or alloys (V for V, andradite for Ca, hematite for
211 Fe, albite for Si, apatite for P, zircon for Zr, UO_2 for U, MnTiO_3 for Mn and Ti, Al_2O_3 for Al, ThO_2 for Th, PbS
212 for Pb and YPO_4 for Y). The analytical conditions were 20 nA current, accelerating voltage of 20 kV and
213 counting time of 10 s. For chlorite, the calibration was also based on natural and synthetic oxides and/or alloys
214 (V for V, andradite for Ca, orthose for K, hematite for Fe, albite for Si and Na, olivine for Mg, MnTiO_3 for Mn
215 and Ti, Al_2O_3 for Al, and Cr_2O_3 for Cr). The analytical conditions were 12 nA current, accelerating voltage of 15
216 kV and counting time of 10 s. The limits of detection of each analysed element are presented in Table SM2
217 (uraninite) and Table SM12 (chlorite).

218 3.3. U-Pb isotopic ages of uranium oxides and apatite

219 SIMS is an established approach to date apatite (Li et al. 2012; Zhou et al. 2018) and uranium oxide (Fayek et al.
220 2000, 2002; Luo et al. 2015; Martz et al. 2019). The U-Pb and Pb/Pb analyses were carried out at the Centre de
221 Recherches Pétrographiques et Géochimiques (CRPG, Nancy, France) with the Cameca IMS 1280 HR2 and the
222 Hyperion RF O^- source for apatite and with the Cameca IMS 1270 E7 and the duoplasmatron O^- source for
223 uranium oxide. The secondary positive ions were measured with a mass resolution ($M/\Delta M$) of 6000 to separate
224 peaks of interest from isobaric interferences, by ion counting in mono-collection mode on the axial electron
225 multiplier.

226 For apatite, the primary O⁻ beam was set at an intensity of 30nA with a 10 μm spot size. Each measurement
227 consisted of a 120 s pre-sputtering, secondary beam and mass centring and 16 cycles of measurement of masses:
228 178.5 (background), ⁴⁰Ca⁴⁴Ca³¹P¹⁶O₄, ²⁰⁴Pb, ²⁰⁶Pb, ²⁰⁷Pb, ²⁰⁸Pb, ²³⁸U, ²³²Th¹⁶O and ²³⁸U¹⁶O. Counting times were
229 4 s per peak for ²³²Th¹⁶O and ²³⁸U¹⁶O, 6 s per peak for ²³⁸U, 8 s per peak for ²⁰⁸Pb and 18 s per peak for ²⁰⁴Pb,
230 ²⁰⁶Pb and ²⁰⁷Pb. An energy window of 30 eV was used with no energy offset. ⁴⁰Ca⁴⁴Ca³¹P¹⁶O₄ was used as a
231 reference mass to calculate the U and Pb contents. The Madagascar apatite was used as standard to determine the
232 relative ionization yield of U and Pb, with the Pb/U ratio expressed as a function of UO/U ratio. The external
233 error on the ²⁰⁶Pb/²³⁸U ratios, measured on the Madagascar standard (dated at 473.5 Ma, Chew et al. 2019) for
234 each session, was propagated on the final error of each sample measurements. With the measurement of the ²⁰⁴Pb
235 isotope it is possible to calculate ²⁰⁶Pb/²³⁸U corrected ages using the measured ²⁰⁴Pb/²⁰⁶Pb ratios and the
236 continental common lead compositions from Stacey and Kramers (1975) at the age of crystallisation. This allows
237 us to calculate probability density plots and weighted average plots using ²⁰⁶Pb/²³⁸U corrected ages, and compare
238 them to the common lead uncorrected Tera-Wasserburg intercept ages (Tera and Wasserburg 1972). All data
239 were treated using ISOPLOT software (Ludwig 2007).

240 For uranium oxides, the primary O⁻ beam was set at an intensity of ~5 nA and focussed to a spot of ~15 μm in
241 diameter, in Gaussian mode with a raster of 10μm. The energy window was opened at 30 eV and centred on the
242 low energy side, 5 eV below the maximum value. An offset of -50eV was applied during analyses in order to
243 avoid matrix effects due to mixes between uraninite and silicate in natural samples. Ions were measured by peak
244 jumping in monocollection mode using the axial Faraday cup (FC) for ²³⁸U and ²³⁸UO and the axial electron
245 multiplier (EM) for ²⁰⁴Pb, ²⁰⁶Pb, ²⁰⁷Pb, ²⁰⁸Pb and ²³²ThO. Each analysis consisted of 8 successive cycles. Each
246 cycle began with measurement of the mass 203.5 and 203.6 for backgrounds of the FC and the EM. The
247 counting time was 4 s for 203.5, 203.6, ²⁰⁸Pb and ²³⁸UO; 3 s for ²⁴⁸ThO; 6 s for ²⁰⁶Pb and ²³⁸U; 10 s for ²⁰⁴Pb and
248 20 s for ²⁰⁷Pb (waiting time of 1 s). The standard used was a uraninite from Zambia (Holliger 1988), which has a
249 given concordant age at 540 ± 4 Ma (Cathelineau et al. 1990). Ages and error correlations were calculated using
250 ISOPLOT (Ludwig 2007). Uncertainties in the ages are reported at the 2σ level. Common Pb corrections were
251 based on the measured ²⁰⁴Pb content using the Pb isotope composition calculated from Stacey and Kramers
252 (1975) at the inferred age of the uranium oxide crystallisation.

253 3.4. Minor and trace element concentrations in uranium oxides

254 Minor and trace elements in uranium oxides, including rare earth elements (REEs), were measured with a Laser
 255 Ablation-Inductively Coupled Plasma-Mass Spectrometer (LA-ICP-MS) at the GeoRessources laboratory
 256 (Nancy, France). The uranium oxides were ablated using a 193 nm Geolas Q Plus system with an aperture-
 257 imaged Complex 103 ArF excimer laser (Microlas, Göttingen, Germany) equipped with beam homogenisation
 258 optics. The laser spot sizes were 16 and 24 μm and the fluence was $\sim 5 \text{ J/cm}^2$ with a repetition rate of 5 Hz.
 259 Ablated particulate material was analysed by an Agilent 7500c Quadrupole ICP-MS. The transport gas was a
 260 mixture of He and Ar, at typical flow rates of 0.5 and 0.8 $\text{l}\cdot\text{min}^{-1}$ respectively. All data were acquired in raw
 261 counts using time-resolved mode. Data reduction was done using Iolite software (Paton et al. 2011). Absolute
 262 concentrations and limits of detection were obtained from the equation developed by Longerich et al. (1996).
 263 The calibration material (external standard) was a SRM NIST 610 glass standard and SRM NIST 612 glass was
 264 analysed to control the precision and accuracy of the measurements (concentrations from Jochum et al. 2011).
 265 The methodology was modified from Lach et al. (2013). The matrix effects when quantifying the REEs in a
 266 uraninite using SRM NIST 612 are limited ($< 15\%$; Lach et al. 2013) and are considered to be in the same range
 267 for the other measured minor and trace elements in the present study, as previously proposed by Frimmel et al.
 268 (2014) and Alexandre et al. (2016). A series of 37 elements were analysed for each experiment: ^{11}B , ^{47}Ti , ^{51}V ,
 269 ^{53}Cr , ^{55}Mn , ^{59}Co , ^{60}Ni , ^{63}Cu , ^{66}Zn , ^{69}Ga , ^{75}As , ^{88}Sr , ^{89}Y , ^{90}Zr , ^{93}Nb , ^{95}Mo , ^{121}Sb , ^{137}Ba , the 14 REEs, ^{181}Ta , ^{182}W ,
 270 ^{209}Bi , ^{232}Th and ^{238}U . ^{238}U was the internal standard measured by EPMA and the used concentration was adjusted
 271 depending of the analysed sample: 77.1 wt% U for WDD07-2 55.9A, 76.8 for WDD07-2 55.9B, 75.6 for
 272 WDD10-151 29.4, 75.2 for WDD08-106 10.6, 74.9 for WDD07-2 73.5B and 72.1 for JDD08-003 74.4B. The
 273 analytical precision calculated for all elements using standard deviation of recorded intensity is better than \pm
 274 20%. The limit of detection (LOD) varies for each element and each analysis as a function of signal intensity and
 275 was calculated for each ablation from signal intensities using the 3σ criterion (Longerich et al. 1996). The LODs
 276 were reported in Table SM3 when the calculated values for a given element fell below these values. Values used
 277 to calculate $(\Sigma\text{LREE}/\Sigma\text{HLREE})_{\text{N}}$ are chondrite-normalised with chondrite values from Anders and Grevesse
 278 (1989) and the following elements were used for calculation:
 279 $\Sigma\text{REE}=\text{La}+\text{Ce}+\text{Pr}+\text{Nd}+\text{Sm}+\text{Eu}+\text{Tb}+\text{Dy}+\text{Ho}+\text{Er}+\text{Tm}+\text{Lu}$;
 280 $(\Sigma\text{LREE}/\Sigma\text{HREE})_{\text{N}}=(\text{La}_{\text{N}}+\text{Ce}_{\text{N}}+\text{Pr}_{\text{N}}+\text{Nd}_{\text{N}}+\text{Sm}_{\text{N}})/(\text{Er}_{\text{N}}+\text{Tm}_{\text{N}}+\text{Lu}_{\text{N}})$..
 281 Correlations matrices (Tables SM4 – SM9) were generated using the ioGAS software. The chosen criteria for a
 282 positive correlation between two elements was a correlation coefficient higher than 0.9, and lower than -0.9 for
 283 an anti-correlation.

284 4. Results

285 4.1. Paragenesis

286 The paragenesis presented in this section is based only on the observations from the samples for this study. A
287 combined paragenesis from this study and Polito et al. (2005a) is presented in Fig. 3 and discussed in the
288 “Discussion” section, where the first uranium oxide generation (U1) and the third one (U3) are presented. In the
289 mineralised intercepts, the early diagenesis is represented by hematite (H1) crystallisation and quartz
290 overgrowths (Q1) on detrital quartz (Q0) grains (Fig. 4a). This was followed by an episode of dissolution of
291 detrital quartz Q0, noted as Q^r in Fig. 4b, in relation to peak diagenesis. Chlorite in rosette-shape (C1, Fig. 4c),
292 rutile (R1, Fig. 4d), clays minerals (dickite D1 and illite I1) and apatite (Ap; mostly 10–20 µm in width, Fig.5a)
293 form during this stage. Chlorite C1 is altered into clay minerals (I1, Fig. 4e). A second generation of quartz (Q2,
294 Fig. 4f) occurs at the end of this stage. A second generation of uranium oxide (U2) crystallises in contact with
295 apatite (Ap) in voids produced by quartz dissolution (Fig. 5a). The U2 postdates apatite as U2 fills small
296 fractures within apatite grains and surrounds them. Veins containing quartz (Q3), uraninite (U4), pyrite (Py3)
297 and chalcopyrite (ccp) crosscut the sandstone (Fig. 5c) and they are thought to be coeval with U4 emplaced in
298 voids (Fig. 5b) based on dating results. A fifth (U5) and sixth (U6) generations of uranium oxide occur (Fig. 5d),
299 filling voids. The mineral assemblage is similar for three last uranium generations, but the ages obtained account
300 for the different generations.

301 4.2. Chemical composition of the uranium oxides

302 The chemical composition of the different uranium oxides are reported in Table SM2 for the major elements and
303 in Table SM3 for minor and trace elements. Fig. 6 shows the chemical maps obtained by EPMA, on which the
304 scales were determined using element concentrations measured during *in-situ* spot EPMA analyses.

305 *Major elements*

306 The U contents of the different generations of uranium oxides range from 63.2 to 90.15 wt% UO₂. The thorium
307 contents for all the uranium oxides is low with concentrations below the detection limits (0.1 wt% Th). The
308 different uranium oxides are characterised by variable contents of Pb, either between samples or within an
309 individual sample (Figs. 6 and 7a). For each sample, the maximum Pb content, corresponding to the least altered
310 zones, and the minimum Pb content which is measured in the most altered ones, are summarized in Table SM2.

311 The samples WDD10-151 29.4 (U4) and WDD08-106 10.6 (U5) have the most homogeneous Pb contents and
312 can be considered as the least altered. The Ti contents are below the detection limit (0.07 wt% TiO₂) except for
313 samples JDD08-003 74.4B (U2) with concentrations up to 1.39 wt% TiO₂, WDD07-2 55.9A and WDD07-2
314 55.9B (U4) up to 2.6 wt% TiO₂ and WDD07-2 73.5B (U6) up to 1.25 wt% TiO₂. The P contents are lower than 2
315 wt% P₂O₅ in sample WDD07-2 73.5B (U6), but can reach 6.93 wt% P₂O₅ in zones where U concentrations are
316 low in samples WDD07-2 55.9A and WDD07-2 55.9B (U4). The calcium and silica contents are also highly
317 variable, ranging from 0.98 to 4.16 wt% CaO with the highest values found in sample JDD08-003 74.4B (U2),
318 WDD07-2 55.9A and WDD07-2 55.9B (U4), and from < LOD (0.1 wt% SiO₂) to 13.11 wt% SiO₂ in zones with
319 low U concentrations. The silica contents are higher than the calcium contents for all the samples except
320 WDD08-106 10.6 (U5). The alteration for samples WDD07-2 55.9A, WDD07-2 55.9B (U4) and WDD07-2
321 73.5B (U6) is marked by a loss in lead compensated by a gain in Si, Ca, Fe and P (Fig. 7a), which is not
322 observed for the other samples.

323 *Minor and trace elements*

324 Among all the minor and trace elements measured by LA-ICP-MS, 14 have contents below the limit of detection
325 (LOD) for some of the analyses. Table SM3 presents the results, with the minimal and maximal values for each
326 sample, and the maximum LOD value calculated for each element considering all samples and all analyses. The
327 diagrams comparing the contents in As, Nb, W, Ba and V (Fig. 7 b, c, d) demonstrate that the different uraninite
328 generations are chemically distinct. Arsenic contents are low in sample WDD07-2 73.5B (U6, 807–4870 ppm),
329 range between 2490 and 5130 ppm for WDD07-2 55.9A (U4), and the highest values are obtained in sample
330 JDD08-003 74.4B (U2, 5750–17590 ppm), WDD10-151 29.4 (U4, 14300–25800 ppm) and WDD08-106 10.6
331 (U5, 10120–13130 ppm, Fig. 7b and Table SM3). Niobium contents range between 5.6 and 137 ppm for JDD08-
332 003 74.4B (U2), between 78.2 and 147.8 ppm for WDD07-2 55.9A (U4), between 6.3 and 16.9 ppm for
333 WDD10-151 29.4 (U4), between 1.56 and 2.7 ppm for WDD08-106 10.6 (U5), and between 0.24 and 108.8 ppm
334 for WDD07-2 73.5B (U6). Tungsten contents range between 67.3 and 156.6 ppm for WDD10-151 29.4 (U4 in
335 veins) and between 551 and 8350 ppm for the other samples. Barium contents range between 227 and 2280 ppm
336 for JDD08-003 74.4B (U2), between 101 and 283 ppm for WDD10-151 29.4 (U4), between 32.6 and 856 ppm
337 for WDD07-2 55.9A (U4), between 69.4 and 77.6 ppm for WDD08-106 10.6m (U5), and between 584 and 7780
338 ppm for WDD07-2 73.5B (U6). Vanadium contents range between 469 and 1637 ppm for WDD07-2 55.9A
339 (U4), and between 1418 and 16510 ppm for JDD08-003 74.4B (U2), WDD10-151 29.4 (U4 in veins), WDD08-
340 106 10.6 (U5), and WDD07-2 73.5B (U6).

342 The REE chondrite-normalised patterns of the uranium oxides from the different samples are variable, but are all
343 characterised by a relatively high concentrations in REEs (between 537 and 40169 ppm Σ REE, Fig. 7e) and an
344 enrichment in LREE and MREE compared to HREE. The REE patterns are homogeneous for a given sample,
345 except for samples JDD08-003 74.4B, WDD07-2 55.9A and WDD07-2 55.9B (Fig. 8). The sample JDD08-003
346 74.4B (U2) is marked by a variation of MREE and HREE (1709 to 42014 ppm Gd and 154 to 6778 ppm Lu for
347 example), whereas sample WDD07-2 55.9A and WDD07-2 55.9B (U4) are marked by a variation of LREE (19
348 to 2493 ppm La for example). Increased LREE contents correlate to higher degrees of alteration in samples
349 WDD07-2 55.9A and WDD07-2 55.9B, whereas no link between alteration and MREE and HREE variations
350 could be established in sample JDD08-003 74.4B. Some of the samples display a negative Eu anomaly
351 (WDD07-2 55.9A and WDD07-2 55.9B, WDD10-151 29.4, WDD07-2 73.5B).

352 *Correlations between elements*

353 Some minor and trace elements are correlated in all the samples, whereas some others are only correlated in
354 some of the uraninite generations. The correlation matrices are presented in Tables SM4–SM9. In all samples the
355 following elements have a positive correlation: Co and Ni; the REEs; and Ba and Ga. In sample JDD08-003
356 74.4B, B is correlated to V, Zn, Ga and Ba; Mn is anti-correlated to the REEs; Bi is correlated to Co and Ni
357 (Table SM4). In sample WDD07-2 55.9A, V is correlated to Ba and the LREE; Mn to Sb; Cu to Ga, Sr and Ba
358 (Table SM5). In sample WDD07-2 55.9B, the REEs, Zr and Th are correlated; B is correlated to Mn and Sb, and
359 anti-correlated to Sr (Table SM6). In sample WDD10-151 29.4, B is correlated to the REEs but anti-correlated to
360 V and Mn (Table SM7). In sample WDD08-106 10.6, As is correlated to the HREE and W, and anti-correlated
361 to V, Mn and Co; Mo is anti-correlated to the LREE (Table SM8). In sample WDD07-2 73.5B, Co is correlated
362 to Cu and Ga; Ti to Nb; B to Co; Ba to Ga and Sr (Table SM9).

363

364 4.3. Isotopic ages of apatite and uranium oxides

365 *Apatite*

366 Apatite predates uranium oxides, as observed in sample JDD08-003 74.4B (Fig. 9a). A significant number of
367 analyses present anomalous U and/or Pb contents correlated to anomalous Pb/Pb or U/Pb ratios (Table SM10
368 and Fig. 9b). These anomalous values are probably linked contribution from uraninite U2 during the analyses of

369 some apatite grains, due to the relatively small size of the apatite grains. When discarding such data, the eight
370 remaining analyses are marked by variable concentrations of common Pb and degrees of discordance, with
371 $^{204}\text{Pb}/^{206}\text{Pb}$ and $^{207}\text{Pb}/^{206}\text{Pb}$ ratios ranging respectively from 0.0015 to 0.0350 and 0.1281 to 0.5846 (Table
372 SM10). The analyses plot in a discordant position on a Tera-Wasserburg diagram with the calculated lower
373 intercept giving a poorly-defined age of 1685 ± 65 Ma (MSWD=1.4; 8 data points).

374 *Uranium oxides*

375 The data for the different uranium oxides dated in this study are given in Table SM11. The majority of the U-Pb
376 isotopic ratios are discordant in the Wetherill Concordia diagram (Fig. 10), indicating that all the uranium oxides
377 suffered from post-crystallisation alteration. The least altered zones (i.e. richest in Pb) were selected for the
378 isotopic dating based on EPMA analyses and mapping (Fig. 6). All the uranium oxides have a contribution of
379 common lead, with $^{204}\text{Pb}/^{206}\text{Pb}$ ratios varying between 0.000001 and 0.001926. Sample WDD10-151 29.4 (U4)
380 has the highest common lead contribution, with $^{204}\text{Pb}/^{206}\text{Pb}$ ratios between 0.000763 and 0.0011327, followed by
381 samples JDD08-003 74.4B (U2, $^{204}\text{Pb}/^{206}\text{Pb}$: 0.000002–0.001926), WDD07-2 55.9A and WDD07-2 55.9B (U4,
382 $^{204}\text{Pb}/^{206}\text{Pb}$: 0.000010–0.000171), WDD08-106 10.6 (U5, $^{204}\text{Pb}/^{206}\text{Pb}$: 0.000030–0.000057) and WDD07-2 73.5B
383 (U6, $^{204}\text{Pb}/^{206}\text{Pb}$: 0.000003–0.000122). All the analyses were corrected for common lead using the common lead
384 contribution calculated at their crystallisation age: 1030 Ma for JDD08-003 74.4B (U2), 730 Ma for WDD10-
385 151 29.4 and WDD07-2 55.9A and WDD07-2 55.9B (U4), 550 Ma for WDD08-106 10.6 (U5), and 350 Ma for
386 WDD07-2 73.5B (U6).

387 The 54 analyses of the uranium oxides from sample JDD08-003 74.4B (U2) are moderately to strongly
388 discordant and give an upper intercept at 1035 ± 57 Ma and a lower intercept at the origin, indicating a recent
389 alteration event (Fig. 10a). The data are scattered with a MSWD of 76, with a majority of analyses with U/Pb
390 ratios close to the origin.

391 The uranium oxides from samples WDD07-2 55.9A and WDD07-2 55.9B (U4) give a global upper intercept age
392 at 661 ± 39 Ma (49 analyses, lower intercept: 12 ± 11 Ma) but the data are highly scattered (MSWD = 170) and
393 present highly variable discordancy behaviour, from almost concordant to strongly discordant (Fig. 10b). When
394 using the less discordant data (25 analyses), the data are less but still scattered (MSWD = 84), with an upper
395 intercept age at 738 ± 44 Ma and a lower intercept at 79 ± 45 Ma.

396 The 20 analyses of the uranium oxides from sample WDD10-151 29.4 (U4) are discordant but grouped (MSWD
397 = 4.2) and give an upper intercept at 725 ± 23 Ma when anchoring the lower intercept at 0 ± 5 Ma (initial
398 calculated lower intercept at -14 ± 6 Ma, Fig. 10c).

399 The 59 analyses of the uranium oxides from sample WDD08-106 10.6 (U5) are discordant but grouped (MSWD
400 = 4.2) with an upper intercept at 554 ± 6 Ma when anchoring the lower intercept at 0 ± 5 Ma (initial calculated
401 lower intercept at -16 ± 15 Ma, Fig. 10d).

402 The 85 analyses of the uranium oxides from sample WDD07-2 73.5B (U6) are highly scattered (MSWD = 139)
403 and present a variable discordancy degree, giving an upper intercept of 350 ± 21 Ma when anchoring the lower
404 intercept at 0 ± 5 Ma (Fig. 10e).

405 All the samples except two (WDD07 2 55.9A and WDD07-2 55.9B) are characterised by a lower intercept at
406 almost 0 Ma, indicating that alteration of the uranium oxides is recent.

407 4.4. Chlorite composition and crystallisation temperatures

408 All the analysed chlorite grains have high iron contents (30.26–45.31 wt% FeO), low magnesium contents (2.01–
409 11.99 wt% MgO), and plot along the Fe^{2+} – Mg^{2+} chamosite–clinochlore substitution trend (Fig. 11a). Silica
410 content ranges from 21.14 to 27.44 wt% and Al between 16.18 and 22.15 wt% Al_2O_3 . Titanium, Mn, Ca, Na and
411 K contents are consistently below detection limits except when chlorite is mixed with illite (Table SM12).
412 Chlorite has a chamositic composition (Fig. 11b, Polito et al. 2005a; this study). To estimate temperature, the
413 model developed by Bourdelle et al. (2013) was used because it was designed for diagenetic to low-grade
414 metamorphic conditions and it avoids the problem of estimating the oxidation state of iron in chlorite. The
415 results are presented in Table SM12, where the "Linear T°" column corresponds to the basic linear model for
416 $T^\circ < 350$ °C, the "Quadratic T°" is based on a quadratic equation used above 350 °C, and the "Final T°"
417 column gives the linear T° when it is below 350 °C and the quadratic one for temperatures above 350 °C. On 99
418 analyses, 13 range between 159 and 300 °C, most of the calculated temperatures are above 300 °C and 42
419 analyses could not be processed due to the sum of $\text{Si} + \text{Ti} + \text{Al} + \text{Fe}^{2+} + \text{Mn} + \text{Mg} + \text{Ca} + \text{Na} + \text{K} - 4$ (in *apfu*)
420 higher than 6. Other thermometers were tested such as the ones developed by Cathelineau (1988) and by Jowett
421 (1991) that also gave calculated temperatures higher than 300 °C.

422 5. Discussion

423 5.1. Timing of the U mineralisation in the Westmoreland area and its correlation 424 to the geodynamic evolution of Australia

425 The paragenesis defined during this study is based on eight representative samples from the mineralised areas of
426 the Redtree, Junnagunna and Huarabagoo U deposits and was combined with the results of Polito et al. (2005a),
427 because the latter paragenetic sequence takes into account a larger diversity of samples from barren, altered and
428 mineralised zones (Fig. 3). Some of their mineral assemblages were not observed in this study, mainly Fe-, Ti-
429 oxides in the detrital minerals, dickite (D1) and pyrite (P1) linked to the ca. 1680 Ma diagenetic event. In the
430 present study, the dickite was not identified and the clay mineral replacing chlorite C1 was illite. A first
431 generation of micron-sized grains of uranium oxide U1 (referred to as “uraninite” in Polito et al. 2005a) is
432 texturally associated with illite I2, hematite H2 and rutile R2. Polito et al. (2005a) described another generation
433 of uranium oxide (noted U3 in the combined sequence) that crystallised in voids or in veins, possibly associated
434 with pyrite (Py2) and galena. These two generations of uranium oxides were not observed in this study.

435 The U-Pb isotopic ages for the uranium oxides range from 1035 ± 57 Ma (sample JDD08-003 74.4B) to $350 \pm$
436 21 Ma (WDD07-2 73.5B), with 4 distinct stages at ca. 1035 Ma, 730 Ma, 550 Ma and 350 Ma (Fig. 10). These
437 ages are younger than the oldest ages calculated for the Westmoreland area on very fine-grained intergranular
438 uraninite U1 inclusions (6–8 μ m) in hematite at Redtree, with $^{207}\text{Pb}/^{206}\text{Pb}$ ages of 1606 ± 80 Ma and 1655 ± 83
439 Ma from two analyses obtained by LA-HR-ICPMS (Polito et al. 2005a). Although the common lead contribution
440 in U1 was not measured, this old age is younger than, but falls within error of the 1680 ± 21 Ma $^{40}\text{Ar}/^{39}\text{Ar}$ age
441 measured for diagenetic illite extracted from the Westmoreland Conglomerate (Polito et al. 2005a) and the 1685
442 ± 65 Ma age measured for apatite in association with uranium oxides at the Junnagunna deposit (sample JDD08-
443 03 74.4B; Fig. 9). Therefore, it can be proposed that a diagenetic or hydrothermal fluid event was active in the
444 area at ca. 1680 Ma, during which clay minerals, apatite and a first stage of uranium oxide crystallised. However,
445 as the U1 ages are younger than the age of the illite and apatite, and considering the associated errors, U1 could
446 also have formed shortly after this major fluid event, or at the end of it. From a geodynamic point of view, the
447 ca. 1680 Ma period in the Westmoreland area can be correlated to the onset of magmatism in the Warumpi
448 Province (Scrimgeour et al. 2005) and to a phase of rifting and intrusion of the 1678 Ma Carters Bore Rhyolite
449 and 1670 Ma syn-extensional Sybella Batholith in the Mount Isa Province (Gibson et al. 2016). This stage was
450 followed by at least five successive events of U mineralisation at ca. 1035 Ma, 870 Ma (Polito et al. 2005a), 730

451 Ma, 550 Ma and 350 Ma, the ages evaluated in this study correlating with the younger events of Polito et al.
452 (2005a, Fig. 10f). These events could either have remobilised pre-existing mineralisation or a new stock of
453 uranium could have been brought to the deposit site, and these two possibilities are discussed in section 5.2.
454 Hypotheses can relate these events to the geodynamic evolution of the McArthur Basin or Australia in a more
455 global view. The timing of the ca. 1035 Ma event corresponds to the 1085–1040 Ma Giles Event, which included
456 a failed east-trending intracontinental rift in the western Musgrave Province and the extensive 1075 Ma
457 Warakurna Large Igneous Province (Wingate et al. 2004; Evins et al. 2010; Howard et al. 2011; Ahmad and
458 Munson 2013). The ca. 870 Ma event corresponds to initiation of the Centralian Superbasin at about 840 Ma
459 related to extension, rifting and crustal sagging that may have been an early expression of the breakup of the
460 Neoproterozoic Rodinia Supercontinent (Lindsay 2002; Greene 2010). The 730 Ma phase corresponds to a
461 period of tectonic quiescence, with little evidence for major tectonic events (Ahmad and Munson 2013). As all
462 the other ages can be correlated with major tectonic events, it can be proposed that a same situation is valid for
463 730 Ma: a currently undefined geodynamic event favoured U mobility. The last two uraniferous events (ca. 550
464 and 350 Ma) take place when central Australia was affected by major intraplate tectonism, that dissected the
465 Centralian Superbasin, exhumed rocks from deep crustal levels, and resulted in large amplitude east-trending
466 gravity anomalies in central Australia (Ahmad and Munson 2013). The first of these events, the Petermann
467 Orogeny, was focused in the Musgrave Province at 580–530 Ma and overlaps to the ca. 550 Ma event. Then, the
468 Alice Springs Orogeny was a major intraplate orogenic event that variably affected large areas of central
469 Australia from 450 to 300 Ma and resulted in the exhumation of the Arunta Region (Collins and Teyssier 1989;
470 Haines et al. 2001) which could be related to the ca. 350 Ma mineralisation. The temporal correlation between
471 the ages of the different uranium oxides in the Westmoreland area and successive geodynamic events having
472 affected Australia demonstrates that these events favoured fluid circulations in the McArthur Basin and related
473 basement, and uranium mobility during more than 1.3 Ga. However, none of the uraninite generations identified
474 so far record the Isan Orogeny (1640–1490 Ma, with the peak around ca 1590 Ma, Murphy et al. 2011) that
475 affected the nearby Mount Isa Basin.

476 5.2. **Geochemistry of the successive U mineralisation: changing physico-chemical** 477 **conditions in the Westmoreland area**

478 The chemical composition of the ca. 1680 Ma uranium oxide U1 (“uraninite” in Polito et al. 2005a) is unknown,
479 precluding comparison with later generations. The chemical compositions of the different generations of
480 uranium oxides identified during this study are specific for each sample in terms of chondrite-normalised REE

481 patterns and minor to trace element concentrations (Figs. 7 and 8). Such results indicate at first order that the
482 physico-chemical conditions for the formation of these different uranium oxides were different (Mercadier et al.
483 2011b; Frimmel et al. 2014; Alexandre et al. 2015). Although the origin of this variability is not precisely
484 constrained (i.e., the chemical composition of the mineralising fluids, the source(s) of the fluids or of the metals,
485 or the pressure-temperature conditions; see Mercadier et al. 2011b), such variability suggests that the physico-
486 chemical conditions within the studied deposits have not been constant through time. The successive generations
487 of uranium oxides do not show any U-Pb isotopic signatures that indicate that they have been altered and/or
488 remobilised by later fluid events; all the lower intercepts of the Discordia lines are younger than 100 Ma (Fig.
489 10). When combined with the variability in the geochemical signatures of the different generations of uranium
490 oxides, these results do not allow conclusively define if U in the Westmoreland area was deposited at ca. 1680
491 Ma then locally remobilised during five fluid events under different conditions, or if each successive fluid event
492 brought a new batch of uranium and related metals to the deposits. The latter option is preferred, as
493 remobilisation of primary uranium in Canadian unconformity-related deposits leads to the formation of uranium
494 oxides in which some of the geochemical markers, like REE patterns, are preserved across the generations
495 (Mercadier et al. 2011a; Martz et al. 2019). The significant variations in the geochemical signatures of the
496 uranium oxides probably indicate new U inputs for each successive generation. In addition to unique chemical
497 signatures, each U-forming event in the Westmoreland area is characterised by a specific mineral assemblage
498 that reflects different formation conditions, or degrees of post-ore alteration (Polito et al. 2011). The U
499 mineralisation currently observed in the Westmoreland area is thus the result of a protracted history spanning at
500 least 1.3 Ga (1.68 to 0.35 Ga) of fluid circulations for which the physico-chemical conditions have varied, in
501 response to specific geodynamic events.

502 5.3. **Chemical composition of the clay minerals and related temperature of** 503 **crystallisation**

504 Published data on C1 chlorite from the Westmoreland U deposits indicate that this unique generation of chlorite
505 is Fe-dominated but has variable Al contents and Mg/Fe ratios depending on their location (Westmoreland
506 Conglomerate and Seigal Volcanics), plotting between the chamosite, clinocllore and Mg-amesite compositions
507 (Fig. 11b; Polito et al. 2005a). The variation in chemical composition leads to variable range of calculated
508 temperatures of formation from 196 °C to 364 °C with the Cathelineau and Nieva (1985) and Cathelineau (1988)
509 methods (Polito et al. 2005a); and from 110 °C to 406 °C with the Bourdelle et al. (2013) method used for this
510 study. All the new analysed C1 chlorite, regardless of the location or deposit, lie in the chamosite field with

511 related temperature of formation mostly above 300 °C (Fig. 11, Table SM12). Polito et al. (2005a) proposed that
512 the Fe-rich composition of the chlorite yielding the highest temperatures of crystallisation (364 °C) was linked to
513 the proximity of the Seigal Volcanics that provided excess Fe during crystallisation of the chlorite. In addition,
514 the Fe²⁺ in the Fe-rich chlorite adjacent to the mafic dykes and volcanic or mafic rocks themselves may have
515 been the chemical reductant that reduced the hexavalent uranium to precipitate uraninite (Wall 2006;
516 International Atomic Energy Agency 2018a). The distance between our samples and the Seigal Volcanics is
517 unknown, but the same process could have resulted in the high Fe contents and the high temperature of
518 crystallisation. Temperature estimates from fluid inclusions in the Redtree, Junnagunna and Huarabagoo deposits
519 are lacking, but fluid inclusions were analysed from two related U deposits (Eva Mine and Jackson Pit) in the
520 basement below the Westmoreland Conglomerate (Mernagh and Wygralak 2011). Based on their description and
521 relation to other minerals, we assume that the quartz veins in which the fluid inclusions were studied are
522 genetically comparable to the Q₂ drusy vein described by Polito et al. (2005a) which are co-genetic or post-date
523 C1 chlorite. Temperatures of homogenisation for the different types of fluid inclusions are between 99 to 380 °C,
524 with two populations: 99–270 °C and 190–380 °C (Mernagh and Wygralak 2011). Assuming that data obtained
525 by Mernagh and Wygralak (2011) can be extrapolated to the Redtree, Junnagunna and Huarabagoo deposits,
526 both chlorite and fluid inclusions indicate abnormally high thermal conditions (T>300 °C) during diagenesis at
527 ca. 1680 Ma and reflect three possible origins. Firstly, the high temperatures could be due to a high regional
528 geothermal gradient. Secondly, the fluids could be heated by the Seigal Volcanics whose age is not constrained
529 but could be correlated to ca. 1780 Ma volcanic rocks (Mernagh and Wygralak 2011). Thirdly, fluids heated in
530 the basement could have been injected into the basin. These high thermal conditions were probably short-lived
531 because temperature estimates for illite I1 and illite I2, which post-date chlorite C1 and is co-genetic of U1
532 uranium stage at 1655 Ma, respectively, range from 150 °C to 250 °C (Polito et al. 2005a).

533 The temperature estimates and ages for the first U mineralising event are however loosely-constrained and the
534 possibility that this U stage formed at ca. 1680 Ma in direct relation with the emplacement of the Seigal
535 Volcanics has to be reconsidered, in particular due to spatial correlation between the U mineralisation and Seigal
536 Volcanics (Fig. 2) and the possible older age of the volcanic rocks. Dyke emplacement driving formation of
537 basin-hosted U mineralisation in Proterozoic basins such as McArthur Basin has been proposed for the Matoush
538 and Camie River U deposits in the Otish Basin, Canada (Alexandre et al. 2015; Lesbros-Piat-Desvial et al.
539 2017), with temperatures of formation exceeding 300 °C. Such implications should be studied in more detail for
540 the Westmoreland area.

541 No information regarding the type of alteration, nature of the fluids or temperatures can be currently provided for
542 the five generations of uranium oxides postdating the ca. 1680 Ma U1 of Polito et al. (2005a), as these
543 generations are not genetically associated with clay minerals, and fluid inclusions study in quartz Q3 associated
544 with uraninite U4 are underway. A first-order assessment could be proposed based the REE contents measured in
545 the uranium oxides (Mercadier et al. 2011b; Frimmel et al. 2014; Alexandre et al. 2015; Martz et al. 2019), but
546 must be considered with caution. As Σ REE for U2 (sample JDD08-003 74.4B) formed at ca. 1030 Ma is above 1
547 wt% (Fig. 6e), a temperature estimate > 350 °C is proposed, whereas the following generations of uranium
548 oxides were probably formed at a temperature < 350 °C.

549 **5.4. Comparison between the uranium deposits in the Westmoreland area and** 550 **unconformity-related U deposits**

551 **5.4.1. Comparison at the scale of the McArthur Basin: Westmoreland area vs ARUF**

552 The Alligator Rivers Uranium Field (ARUF) of the McArthur Basin hosts numerous unconformity-related U
553 deposits such as Ranger, Nabarlek, Jabiluka and Koongarra (Polito et al. 2004, 2005b, 2011; Jefferson et al.
554 2007; Cuney and Kyser 2015; Skirrow et al. 2016). As these deposits and those in the Westmoreland area share
555 similar first-order settings and are all associated with the McArthur Basin, it is critical to establish if they could
556 be linked to the same ore-forming events and/or ore-forming processes.

557 Deposits in the ARUF are located exclusively in the basement rocks, near the unconformity between an Archean
558 to Paleoproterozoic basement complex and the McArthur Basin, are structurally-controlled, and have grades
559 mostly above 0.1% U₃O₈ (Rawlings 1999; Jackson et al. 2000). Deposits in the Westmoreland area are
560 structurally-controlled, spatially-related to volcanic dykes and sills in the basin and have lower grades (Hein
561 2002; Polito et al. 2005a; Skirrow et al. 2016; Laramide Resources Ltd 2019).

562 The ARUF and the Westmoreland area were affected by a major diagenetic/hydrothermal fluid circulation event
563 at ca. 1680–1600 Ma (Fig. 12). This episode is recorded in multiple isotopic ages measured on illite, apatite and
564 uranium oxides for the two regions (Maas 1989; Polito et al. 2004, 2005a, b; Clauer et al. 2015; Skirrow et al.
565 2016). The fluids of the diagenetic/hydrothermal event in the ARUF and Westmoreland area at 1680–1600 Ma
566 were basin-derived brines and low-salinity fluids (Ypma and Fuzikawa 1980; Wilde et al. 1989; Derome et al.
567 2003, 2007; Polito et al. 2004, 2005b, 2006; Mernagh and Wygralak 2011). The isotopic and fluid inclusions
568 data at Westmoreland show the involvement of NaCl-rich and CaCl₂-rich brines derived from evaporated
569 seawater, comparable to the two brines related to formation of the unconformity-related deposits in the ARUF

570 (Derome et al. 2007). The mixing between low-salinity fluids and brines is a key process for ore deposition in
571 both areas (e.g. Derome et al., 2003, 2007; Mernagh and Wygralak, 2011). Although contemporaneous and
572 related to the same types of fluids, the fluids at ca. 1680 Ma in the ARUF and Westmoreland area are physico-
573 chemically different based on the differences in the mineralogy and chemistry of the minerals which crystallised
574 at that time in both areas. The most recent studies on unconformity-related U deposits from the ARUF, in
575 particular for the Ranger U deposit, show significant differences with the deposits in the Westmoreland area in
576 terms of the composition of chlorite (Skirrow et al. 2016; Gigon et al. 2019) and the presence and composition of
577 hydrothermal tourmaline (Gigon et al. 2019).

578 The unconformity-related U deposits in the ARUF at ca. 1680–1600 Ma formed through Mg- and B-
579 metasomatism (Fisher et al. 2013; Skirrow et al. 2016; Gigon et al. 2019), but such metasomatism is lacking in
580 the Westmoreland area. The absence of hydrothermal Mg-tourmaline with the uranium oxides in the
581 Westmoreland area is a first striking difference, as this mineral is a pathfinder for unconformity-related U
582 deposits in the ARUF (Skirrow et al. 2016; Gigon et al. 2019). The second difference is the chlorite composition:
583 the chlorite in the Westmoreland area are dominantly chamosite (Fe-rich), compared to the clinoclone to sudoite
584 composition (Mg-rich) of the diagenetic/hydrothermal chlorite in the unconformity-related deposits in the ARUF
585 (Fig. 11b, Polito et al. 2004, 2005b; Beaufort et al. 2005; Gigon et al. 2019). As a consequence, the
586 diagenetic/hydrothermal chlorite composition for the ARUF yields temperatures between 101 °C and 163 °C,
587 with mean temperature of 128 °C and median temperature of 124 °C (Gigon et al. 2019), considerably lower
588 than the > 300 °C calculated in this study.

589 The present study identifies for the first time multiple U generations between 1035 and 350 Ma in three deposits
590 of the Westmoreland area. The succession of fluid events also characterises the unconformity-related U deposits
591 from the ARUF, with multiple ages ranging from 1680 Ma to Present measured on both uranium oxides and illite
592 (Hills and Richards 1976; Ludwig et al. 1987; Maas 1989; Polito et al. 2004, 2005b; Ahmad and Munson 2013;
593 Clauer et al. 2015; Skirrow et al. 2016). These post-1680 Ma ages in the ARUF mainly fall between 1600 and
594 1300 Ma for the clay minerals and some uranium oxides, but are dominantly younger than 900 Ma for the
595 uranium oxides. Based on the available datasets, the post-1680 Ma ages measured for the ARUF do not totally
596 correlate with the five post-1680 Ma ages measured at the Westmoreland area, which could reflect that the fluid
597 events in the two areas are partially disconnected in time from 1680 Ma to Present. The nature of the fluid(s) and
598 physico-chemical conditions of these events in the ARUF are not well constrained.

599 It is currently not possible to link the physico-chemical conditions for the U1 generation in the Westmoreland
600 area with the primary uraninite in the ARUF as no analyses were done on U1. Both primary mineralisation could
601 have been formed in a similar system, but under higher temperature conditions in the Westmoreland area. In this
602 area, the ultimate origin of the different generations and the physico-chemical conditions prevailing between
603 1035 and 350 Ma also remain to be constrained. The chondrite-normalised REE patterns of uranium oxides,
604 which are diagnostic features of deposit types, differ significantly between the ARUF and the Westmoreland
605 area. The different generations of uranium oxides in the Westmoreland area do not exhibit the “bell-shape” (i.e.
606 high concentrations of Tb and Dy) typical of unconformity-related U deposits from the ARUF such as Nabarlek
607 and Koongarra (Mercadier et al. 2011b). Even if some post-crystallisation modification of the REE patterns may
608 have contributed to the LREE enrichment (as described in the Athabasca Basin by Mercadier et al. 2011a and
609 Martz et al. 2019), such phenomenon is not sufficient to explain the major differences of the REE patterns
610 between the two areas. The uranium oxides from the Westmoreland area have significantly higher contents in
611 common lead (Table SM11) when compared to typical uranium oxides from unconformity-related uranium
612 oxides (Skirrow et al. 2016; Martz et al. 2019), which is also an indicator of differences in their conditions of
613 formation. It can be concluded that the formation conditions of the different U generations in the Westmoreland
614 area did not correspond to those known for unconformity-related U deposits in the ARUF.

615 **5.4.2. Comparison between U deposits in the Westmoreland area and U deposits in** 616 **Canadian Proterozoic basins**

617 Several Paleo- to Mesoproterozoic basins in Canada host U mineralisation: the Athabasca Basin (Saskatchewan),
618 the Thelon Basin (Nunavut) and the Otish Basin (Québec).

619 The U mineralisation in the Athabasca Basin is of unconformity-related type, like the one in the ARUF
620 (Jefferson et al. 2007; Cuney and Kyser 2015). The ca. 1680-1600 Ma diagenetic/hydrothermal episode defined
621 in the Westmoreland area is documented in the Thelon Basin, where apatite is dated at 1667 ± 5.1 Ma (Davis et
622 al. 2011). In the Athabasca Basin, this fluid event has been recorded by TIMS analyses of hydrothermal zircon
623 tips (uranium-rich, thorium-depleted) in a leucogranite sampled 200 meters east of the McArthur River high-
624 grade U deposit with ages from 1680 to 1550 Ma. This was interpreted as the approximate timing of the
625 thermotectonic event(s) and associated fluids that produced the new U-rich zircon (Annesley et al. 2007). In
626 addition with the 1650-1700 Ma diagenetic apatite age (Cumming et al. 1987), such results confirm a global
627 fluid event at 1680–1600 Ma affecting the Athabasca, Thelon and McArthur basins which could have belong to
628 the same super basin at that time (Furlanetto et al. 2016). No U mineralisation has however been dated at 1680

629 Ma for the Athabasca and Thelon basins, with maximum ages at ca. 1590 Ma (Alexandre et al. 2009) and ca.
630 1500 Ma (Sharpe et al. 2015) respectively. Recent data on U mineralisation in the Thelon Basin indicate that
631 these deposits had a polyphased history over hundreds of Ma in which unconformity-related U mineralisation
632 formed from ca. 1500 Ma, followed by low-T and meteoric-related redox fronts (Sharpe et al. 2015; Chi et al.
633 2017; Shabaga et al. 2017; Grare et al. 2020).

634 In the Otish Basin, host of the Matoush and Camie River U deposits, no significant hydrothermal activity is
635 known at ca. 1680 Ma. This basin formed earlier than the Athabasca and Thelon basins with a minimum
636 deposition age of 2172 to 2162 Ma (Hamilton and Buchan 2016; Milidragovic et al. 2016). The oldest reported
637 age of fluid circulation and mineralisation is ca. 1725 Ma for the Camie River U deposit (Beyer et al. 2012;
638 Lesbros-Piat-Desvial et al. 2017). This ca. 1725 Ma U mineralisation was initially interpreted to be
639 unconformity-related type (Beyer et al. 2012), but recent research contradicts this interpretation because of a
640 Paleoproterozoic, higher-temperature hydrothermal event, whose origin remains speculative (Lesbros-Piat-
641 Desvial et al. 2017). The timing of formation of the Matoush deposit is loosely constrained (1695 ± 110 Ma;
642 Alexandre et al. 2015), and its main characteristics (spatial association with a dyke, alteration mineralogy,
643 association between uraninite and eskolaite) do not support classification as an unconformity-related type
644 deposit, although the U-bearing fluids were oxidising basinal fluids (Alexandre et al. 2015), like for the
645 Westmoreland area.

646 The chemical composition of uranium oxides analysed in this study records major differences for minor and
647 trace elements (including REEs) compared to typical unconformity-related U deposits from the Athabasca
648 (Mercadier et al. 2011b; Alexandre et al. 2016; Martz et al. 2019) or Thelon basins (Grare et al. 2020). This is
649 particularly visible when comparing the chondrite-normalised REE patterns, as the different generations of
650 uranium oxides from the Westmoreland area do not have the typical bell-shape pattern of the unconformity-
651 related U deposits (Fig. 8). Differences are also visible for numerous minor and trace elements like As, W, Ba
652 and V (Fig. 7c and d) compared with McArthur River and Cigar Lake U deposits of the Athabasca Basin
653 (Alexandre et al. 2015; Martz et al. 2019). The majority of the minor and trace elements have significantly
654 higher concentrations in the uranium oxides from the Westmoreland area, which could indicate a higher
655 temperature of formation and/or different sources of metals. The complete geochemistry of the uranium oxides
656 from the Otish Basin is lacking, but the REE patterns of the ca. 1725 Ma uranium oxides from the Camie River
657 are rather similar to those measured for different generations of uranium oxide from the Westmoreland area (Fig.
658 8). Such results allow consideration that the physico-chemical conditions for the formation of the U

659 mineralisation in the Westmoreland area were probably more similar to those of Matoush or Camie River U
660 deposits of the Otish Basin than those of the Athabasca and Thelon basins. Temperatures estimates from the
661 Matoush (~300 ±50 °C, based on illite and chlorite crystal chemistry, Alexandre et al. 2015) and Camie River
662 deposits (275 to 300 °C, Beyer et al. 2012 and 320 °C, Lesbros-Piat-Desvial et al. 2017) are comparable to the
663 Westmoreland area, but significantly higher than values reported from the Athabasca and Thelon basins (e.g.
664 Kotzer and Kyser 1995; Richard et al. 2016; Chi et al. 2017; Grare et al. 2020).

665 Other similarities with the U deposits from the Otish Basin are the lack of Mg-rich minerals (sidoite, Mg-foitite)
666 or alumino-phosphate-sulfate minerals, which are markers of unconformity-related U deposits. The Matoush and
667 Camie River deposits are spatially related to dykes (Beyer et al., 2012; Alexandre et al. 2015; Lesbros-Piat-
668 Desvial et al. 2017), which played a role as the reductant of uranium, because it was a source of Cr and Fe at
669 Matoush (Alexandre et al. 2015). An equivalent process was proposed for the Westmoreland area with the
670 implication of iron from the dykes as reductant (Polito et al. 2005a). The mafic activity in the Otish Basin and in
671 the southern McArthur Basin (Westmoreland area) could thus have favoured the formation of atypical U
672 deposits, although linked to the same types of fluids as unconformity-related U deposits.

673 **6. Conclusions**

674 The new data provided on U mineralised intercepts from three deposits of the Westmoreland area (Queensland
675 and Northern Territory, Australia) indicate that this region of the McArthur Basin experienced several episodes
676 of fluid circulation between ca. 1680 Ma to Present, which document a protracted mobility of uranium over more
677 than 1.3 Ga. Based on published and new data, six different events of U mobility were active at ca. 1680 Ma,
678 1035 Ma, 850 Ma, 730 Ma, 550 Ma and 350 Ma. The ca. 1680 Ma mineralisation formed due to the circulation
679 and mixing of NaCl-rich, CaCl₂-rich basin-derived brines and low-salinity fluids. The timing and type of fluids
680 involved were comparable to those of the unconformity-related U deposits in the ARUF to the North of the
681 McArthur Basin. The physico-chemical conditions for the formation of these contemporaneous uranium
682 mineralisations are different between the two regions, with higher chlorite temperature (> 300 °C) for the
683 Westmoreland area and absence of Mg- and B-metasomatism typical of unconformity-related U deposits.
684 Although the precise chemical composition of the uranium oxides formed at ca. 1680 Ma has not been measured,
685 all the other U generations found in the Westmoreland area are chemically different from the uranium oxides
686 found in unconformity-related U deposits. The Westmoreland area samples contain higher contents of numerous

687 minor and trace elements, like REEs, which supports a higher temperature of crystallisation. If the timing and the
688 types of fluids between the two parts of the basin were similar at ca. 1680 Ma, fluids in the Westmoreland area
689 were at higher temperatures, driven by a high regional geothermal gradient controlled by volcanism (Seigal
690 Volcanics), or injection of fluids heated in the basement into the basin . This elevated thermal regime may have
691 triggered fluid circulation in the Westmoreland area, with the dykes providing the structural and chemical traps
692 that focused the uranium-bearing brines and favoured U deposition at ca. 1680 Ma. Such conditions appear
693 similar to those known for the formation of U deposits in the Proterozoic Otish Basin (Québec, Canada) at ca.
694 1725 Ma. The new data proposed in this study indicate that the geochemical signature of the successive uranium
695 oxides from the Westmorland area are poorly compatible with uranium oxides formed in unconformity-related U
696 deposits, as confirmed by the difference in mineral association. It is therefore considered as unlikely to find
697 unconformity-related U deposits in this area. The significant changes in the chemical compositions of the
698 different generations of uranium oxides are in favour of changing conditions between 1680 and 350 Ma.
699 Although the precise physico-chemical are loosely defined, the signatures observed in the Westmorland area for
700 the first U stages are closer to those proposed for U deposits from the Otish Basin than those for the Athabasca
701 or Thelon basins.

702

703 **Acknowledgements**

704 The Northern Territory Geological Survey provided logistical support for the sampling mission. Laramide
705 Resources Ltd. provided authorisation, logistical support and guidance for sampling on the Westmoreland
706 exploration camp (especially Adrian Buer and Evan Hughes). Alexandre Flammang and John Moine
707 (GeoRessources Lab) as well as Thin Section Lab company staff are acknowledged for careful thin section
708 preparation. Chantal Peiffert, Andreï Lecomte and Olivier Rouer (GeoRessources Lab) are acknowledged for
709 support in LA-ICP-MS, SEM and EPMA analyses respectively. This research was funded by (i) a French
710 Ministry of Higher Education and Research PhD salary Grant to J.G., (ii) a Région Lorraine-FEDER grant to
711 J.M.: « Rôle des phases fluides dans la distribution spatiale des ressources métalliques dans les bassins
712 sédimentaires paléoproterozoïques australiens », (iii) OSU OTELo grants to J.M. : « Conditions de transport des
713 métaux dans un mégabassin protérozoïque » and A.R. : « Transferts de fluides et métaux dans le bassin de
714 McArthur (Australie) » and (iv) a CNRS-INSU-CESSUR grant to J.M. « Transferts des fluides et métaux dans

715 les méga-bassins paléoprotérozoïques ». The French National Agency through the national program
716 « Investissements d'avenir » of the Labex Ressources 21 (reference ANR-10-LABX-21-RESSOURCES21)
717 partly funded the last developments of the SIMS lab. The comments of David Quirt and an anonymous reviewer
718 greatly helped improving the manuscript. Mostafa Fayek is warmly thanked for careful editorial handling.

719

720

721 **References**

722 Ahmad M (1987) Uranium-gold occurrences of the Murphy Inlier and surrounding region. Northern Territory
723 Geological Survey. Technical Report 87/2

724 Ahmad M, Dunster JN, Munson TJ (2013) Chapter 15: McArthur Basin: in Ahmad M and Munson TJ
725 (compilers). 'Geology and mineral resources of the Northern Territory'. Special Publication 5

726 Ahmad M, Munson TJ (compilers) (2013) Geology and mineral resources of the Northern Territory. Northern
727 Territory Geological Survey/ ISBN 978-0-7245-7257-1

728 Ahmad M, Wygralak A (1989) Calvert Hills, Northern Territory. 1: 250 000 metallogenic map series
729 explanatory notes, SE 53-08. Northern Territory Geological Survey

730 Ahmad M, Wygralak AS (1990) Murphy Inlier and environs—regional geology and mineralisation. Geology of
731 the Mineral Deposits of Australia and Papua New Guinea (editor Hughes FE) The Australasian Institute
732 of Mining & Metallurgy, Melbourne 819–826

733 Alexandre P, Kyser K, Layton-Matthews D, et al (2016) Chemical compositions of natural uraninite. Canadian
734 Mineralogist 53:1–30. <https://doi.org/10.3749/canmin.1500017>

735 Alexandre P, Kyser K, Layton-Matthews D, et al (2015) Formation of the enigmatic Matoush uranium deposit in
736 the Paleoproterozoic Otish Basin, Quebec, Canada. Mineralium Deposita 50:825–845.
737 <https://doi.org/10.1007/s00126-014-0569-5>

738 Alexandre P, Kyser K, Thomas D, et al (2009) Geochronology of unconformity-related uranium deposits in the
739 Athabasca Basin, Saskatchewan, Canada and their integration in the evolution of the basin. Miner
740 Deposita 44:41. <https://doi.org/10.1007/s00126-007-0153-3>

741 Anders E, Grevesse N (1989) Abundances of the elements: Meteoritic and solar. Geochimica et Cosmochimica
742 acta 53:197–214. [https://doi.org/10.1016/0016-7037\(89\)90286-X](https://doi.org/10.1016/0016-7037(89)90286-X)

743 Annesley IR, Madore C, McCready AJ, et al (2007) U-Pb ages of zircon, monazite, and zircon tips in Hudsonian
744 granites at the McArthur River uranium deposit: a record of U mineralizing fluids. In: Proceedings of
745 the Ninth Biennial SGA Meeting. Dublin, pp 1125–1128

746 Beaufort D, Patrier P, Laverret E, et al (2005) Clay alteration associated with Proterozoic unconformity-type
747 uranium deposits in the East Alligator Rivers uranium field, Northern Territory, Australia. Economic
748 Geology 100:515–536

749 Beyer SR, Kyser K, Hiatt EE, et al (2012) Basin Evolution and Unconformity-Related Uranium Mineralization:
750 The Camie River U Prospect, Paleoproterozoic Otish Basin, Quebec. Economic Geology 107:401–425.
751 <https://doi.org/10.2113/econgeo.107.3.401>

- 752 Billault V, Beaufort D, Patrier P, Petit S (2002) Crystal chemistry of Fe-sudoites from uranium deposits in the
753 Athabasca Basin (Saskatchewan, Canada). *Clays and Clay Minerals* 50:70–81.
754 <https://doi.org/10.1346/000986002761002847>
- 755 Bourdelle F, Parra T, Chopin C, Beyssac O (2013) A new chlorite geothermometer for diagenetic to low-grade
756 metamorphic conditions. *Contributions to Mineralogy and Petrology* 165:723–735.
757 <https://doi.org/10.1007/s00410-012-0832-7>
- 758 Cathelineau M (1988) Cation site occupancy in chlorites and illites as function of temperature. *Clay minerals*
759 23:471–85
- 760 Cathelineau M, Boiron MC, Holliger P, Poty B (1990) Metallogenesis of the French part of the Variscan orogen.
761 Part II: Time-space relationships between U, Au and Sn-W ore deposition and geodynamic events—
762 mineralogical and U-Pb data. *Tectonophysics* 177:59–79. [https://doi.org/10.1016/0040-1951\(90\)90274-](https://doi.org/10.1016/0040-1951(90)90274-C)
763 C
- 764 Cathelineau M, Nieva D (1985) A chlorite solid solution geothermometer the Los Azufres (Mexico) geothermal
765 system. *Contributions to Mineralogy and Petrology* 91:235–244
- 766 Chew D, Drost K, Petrus JA (2019) Ultrafast, > 50 Hz LA - ICP - MS Spot Analysis Applied to U–Pb Dating
767 of Zircon and other U- Bearing Minerals. *Geostand Geoanal Res* 43:39–60.
768 <https://doi.org/10.1111/ggr.12257>
- 769 Chi G, Haid T, Quirt D, et al (2017) Petrography, fluid inclusion analysis, and geochronology of the End
770 uranium deposit, Kiggavik, Nunavut, Canada. *Mineralium Deposita* 52:211–232.
771 <https://doi.org/10.1007/s00126-016-0657-9>
- 772 Clauer N, Mercadier J, Patrier P, et al (2015) Relating unconformity-type uranium mineralization of the
773 Alligator Rivers Uranium Field (Northern Territory, Australia) to the regional Proterozoic tectono-
774 thermal activity: An illite K–Ar dating approach. *Precambrian Research* 269:107–121.
775 <https://doi.org/10.1016/j.precamres.2015.08.007>
- 776 Collins WJ, Teyssier C (1989) Crustal scale ductile fault systems in the Arunta Inlier, central Australia.
777 *Tectonophysics* 158:49–66. [https://doi.org/10.1016/0040-1951\(89\)90314-4](https://doi.org/10.1016/0040-1951(89)90314-4)
- 778 Cumming GL, Krstic D, Wilson JA (1987) Age of the Athabasca group, northern Alberta. In: Geological
779 Association of Canada - Mineralogical Association of Canada Joint Annual Meeting, Program with
780 Abstracts. p 35
- 781 Cuney M, Kyser K (2015) Geology and geochemistry of uranium and thorium deposits. Mineralogical
782 Association of Canada. ISBN 0-921294-57-3
- 783 Davis WJ, Gall Q, Jefferson CW, Rainbird RH (2011) Fluorapatite in the Paleoproterozoic Thelon Basin:
784 Structural-stratigraphic context, in situ ion microprobe U-Pb ages, and fluid-flow history. *Bulletin*
785 123:1056–1073
- 786 Derome D, Cathelineau M, Fabre C, et al (2007) Paleo-fluid composition determined from individual fluid
787 inclusions by Raman and LIBS: Application to mid-proterozoic evaporitic Na-Ca brines (Alligator
788 Rivers Uranium Field, Northern Territory Australia). *Chem Geol* 237:240–254.
789 <https://doi.org/10.1016/j.chemgeo.2006.10.015>
- 790 Derome D, Cuney M, Cathelineau M, et al (2003) A detailed fluid inclusion study in silicified breccias from the
791 Kombolgie sandstones (Northern Territory, Australia): inferences for the genesis of middle-Proterozoic
792 unconformity-type uranium deposits. *Journal of Geochemical Exploration* 80:259–275.
793 [https://doi.org/10.1016/S0375-6742\(03\)00194-8](https://doi.org/10.1016/S0375-6742(03)00194-8)
- 794 Durak B, Pagel M, Poty B (1983) Températures et salinités des fluides au cours des silicifications diagénétiques
795 d'une formation gréseuse surmontant un gisement d'uranium du socle: l'exemple des grès Kombolgie
796 (Australie). Paris

- 797 Evins PM, Smithies RH, Howard HM, et al (2010) Redefining the Giles Event within the setting of the 1120–
798 1020 Ma Ngaanyatjarra Rift, west Musgrave Province, Central Australia. Geological Survey of Western
799 Australia, Record 6:36
- 800 Fayek M, Harrison TM, Ewing RC, et al (2002) O and Pb isotopic analyses of uranium minerals by ion
801 microprobe and U–Pb ages from the Cigar Lake deposit. Chemical Geology 185:205–225.
802 [https://doi.org/10.1016/S0009-2541\(01\)00401-6](https://doi.org/10.1016/S0009-2541(01)00401-6)
- 803 Fayek M, Harrison TM, Grove M, Coath CD (2000) A Rapid *In Situ* Method for Determining the Ages of
804 Uranium Oxide Minerals: Evolution of the Cigar Lake Deposit, Athabasca Basin. International Geology
805 Review 42:163–171. <https://doi.org/10.1080/00206810009465075>
- 806 Fisher LA, Cleverley JS, Pownceby M, MacRae C (2013) 3D representation of geochemical data, the
807 corresponding alteration and associated REE mobility at the Ranger uranium deposit, Northern
808 Territory, Australia. Mineralium Deposita 48:947–966. <https://doi.org/10.1007/s00126-013-0463-6>
- 809 Frimmel HE, Schedel S, Brätz H (2014) Uraninite chemistry as forensic tool for provenance analysis. Applied
810 Geochemistry 48:104–121. <https://doi.org/10.1016/j.apgeochem.2014.07.013>
- 811 Fuchs HD, Schindlmayer WE (1981) The Westmoreland uranium deposit, Queensland, Australia. In: Uranium
812 exploration case histories. International Atomic Energy Agency
- 813 Furlanetto F, Thorkelson DJ, Rainbird RH, et al (2016) The Paleoproterozoic Wernecke Supergroup of Yukon,
814 Canada: Relationships to orogeny in northwestern Laurentia and basins in North America, East
815 Australia, and China. Gondwana Research 39:14–40. <https://doi.org/10.1016/j.gr.2016.06.007>
- 816 Gibson GM, Meixner AJ, Withnall IW, et al (2016) Basin architecture and evolution in the Mount Isa mineral
817 province, northern Australia: Constraints from deep seismic reflection profiling and implications for ore
818 genesis. Ore Geology Reviews 76:414–441. <https://doi.org/10.1016/j.oregeorev.2015.07.013>
- 819 Gigon J, Deloule E, Huston DL, et al (2020) Tracing metal sources for the giant McArthur River Zn-Pb ore
820 deposit using Pb-isotopes. Geology: <https://doi.org/10.1130/G47001.1>
- 821 Gigon J, Skirrow RG, Harlaux M, et al (2019) Insights into B-Mg-Metasomatism at the Ranger U Deposit (NT,
822 Australia) and Comparison with Canadian Unconformity-Related U Deposits. Minerals 9:432.
823 <https://doi.org/10.3390/min9070432>
- 824 Grare A, Benedicto A, Mercadier J, et al (2020) Structural controls and metallogenic model of polyphase
825 uranium mineralization in the Kiggavik area (Nunavut, Canada). Miner Deposita.
826 <https://doi.org/10.1007/s00126-020-00957-x>
- 827 Greene DC (2010) Neoproterozoic rifting in the southern Georgina Basin, central Australia: Implications for
828 reconstructing Australia in Rodinia. Tectonics 29:20 p. <https://doi.org/10.1029/2009TC002543>
- 829 Haines PW, Hand M, Sandiford M (2001) Palaeozoic synorogenic sedimentation in central and northern
830 Australia: A review of distribution and timing with implications for the evolution of intracontinental
831 orogens. Australian Journal of Earth Sciences 48:911–928. <https://doi.org/10.1046/j.1440-0952.2001.00909.x>
- 833 Hamilton MA, Buchan KL (2016) A 2169 Ma U–Pb baddeleyite age for the Otish Gabbro, Quebec: implications
834 for correlation of Proterozoic magmatic events and sedimentary sequences in the eastern Superior
835 Province. Canadian Journal of Earth Sciences 53:119–128
- 836 Hein KAA (2002) Geology of the Ranger Uranium Mine, Northern Territory, Australia: structural constraints on
837 the timing of uranium emplacement. Ore Geology Reviews 20:83–108. [https://doi.org/10.1016/S0169-1368\(02\)00054-9](https://doi.org/10.1016/S0169-1368(02)00054-9)
- 839 Hills JH, Richards JR (1976) Pitchblende and galena ages in the Alligator Rivers region, Northern Territory,
840 Australia. Mineralium Deposita 11:133–154. <https://doi.org/10.1007/BF00204477>

- 841 Holliger P (1988) Ages U-Pb définis in situ sur oxydes d'uranium à l'analyseur ionique: méthodologie et
842 conséquences géochimiques. Comptes rendus de l'Académie des sciences Série 2, Mécanique,
843 Physique, Chimie, Sciences de l'univers, Sciences de la Terre 307:367–373
- 844 Hollis JA, Beyer EE, Whelan JA, et al (2010) Summary of results. NTGS laser U-Pb and Hf geochronology
845 project: Pine Creek Orogen, Murphy Inlier, McArthur Basin and Arunta Region, July 2007–June 2008.
846 Northern Territory Geological Survey, Record 1:
- 847 Howard HM, Smithies RH, Evins PM, et al (2011) Explanatory notes for the west Musgrave Province.
848 Geological Survey of Western Australia, Record 4:349
- 849 International Atomic Energy Agency (2018a) Geological classification of uranium deposits and description of
850 selected examples. ISBN 978-92-0-101618-8
- 851 International Atomic Energy Agency (2018b) Unconformity-related uranium deposits. ISBN 978-92-0-108518-4
- 852 Jackson MJ, Scott DL, Rawlings DJ (2000) Stratigraphic framework for the Leichhardt and Calvert Superbasins:
853 review and correlations of the pre-1700 Ma successions between Mt Isa and McArthur River. Aust J
854 Earth Sci 47:381–403. <https://doi.org/10.1046/j.1440-0952.2000.00789.x>
- 855 Jefferson CW, Thomas DJ, Gandhi SS, et al (2007) Unconformity-associated uranium deposits of the Athabasca
856 Basin, Saskatchewan and Alberta. Bulletin / Geological Survey of Canada 588:23
- 857 Jochum KP, Weis U, Stoll B, et al (2011) Determination of reference values for NIST SRM 610–617 glasses
858 following ISO guidelines. Geostandards and Geoanalytical Research 35:397–429.
859 <https://doi.org/10.1111/j.1751-908X.2011.00120.x>
- 860 Jowett EC (1991) Fitting iron and magnesium into the hydrothermal chlorite geothermometer. In:
861 GAC/MAC/SEG Joint Annual Meeting, Toronto, May 27-29, 1991, Program with Abstracts 16
- 862 Knutson J, Ferguson J, Roberts WMB, et al (1979) Petrogenesis of the copper-bearing breccia pipes, Redbank,
863 Northern Territory, Australia. Economic Geology 74:814–826.
864 <https://doi.org/10.2113/gsecongeo.74.4.814>
- 865 Kotzer TG, Kyser TK (1995) Petrogenesis of the Proterozoic Athabasca Basin, northern Saskatchewan, Canada,
866 and its relation to diagenesis, hydrothermal uranium mineralization and paleohydrogeology. Chemical
867 Geology 120:45–89. [https://doi.org/10.1016/0009-2541\(94\)00114-N](https://doi.org/10.1016/0009-2541(94)00114-N)
- 868 Lach P, Mercadier J, Dubessy J, et al (2013) *In Situ* Quantitative Measurement of Rare Earth Elements in
869 Uranium Oxides by Laser Ablation-Inductively Coupled Plasma-Mass Spectrometry. Geostand Geoanal
870 Res 37:277–296. <https://doi.org/10.1111/j.1751-908X.2012.00161.x>
- 871 Lally JH, Bajwah Z (2006) Uranium deposits of the Northern Territory. Northern Territory Geological Survey,
872 Report 20
- 873 Laramide Resources Ltd (2019) Westmoreland Uranium Project website.
874 <https://laramide.com/projects/westmoreland-project/>. Accessed 26 Jun 2019
- 875 Laramide Resources Ltd (2016) Westmoreland Uranium Project - National instrument 43-101; Technical report -
876 scoping study
- 877 Lesbros-Piat-Desvial M, Beaudoin G, Mercadier J, Creaser R (2017) Age and origin of uranium mineralization
878 in the Camie River deposit (Otish Basin, Québec, Canada). Ore Geology Reviews 91:196–215.
879 <https://doi.org/10.1016/j.oregeorev.2017.10.006>
- 880 Li Q-L, Li X-H, Wu F-Y, et al (2012) In-situ SIMS U–Pb dating of phanerozoic apatite with low U and high
881 common Pb. Gondwana Research 21:745–756

- 882 Lindsay JF (2002) Supersequences, superbasins, supercontinents evidence from the Neoproterozoic-Early
883 Palaeozoic basins of central Australia. *Basin Research* 14:207–223. <https://doi.org/10.1046/j.1365->
884 2117.2002.00170.x
- 885 Longerich HP, Jackson SE, Günther D (1996) Inter-laboratory note. Laser ablation inductively coupled plasma
886 mass spectrometric transient signal data acquisition and analyte concentration calculation. *Journal of*
887 *analytical atomic spectrometry* 11:899–904. <https://doi.org/10.1039/JA9961100899>
- 888 Ludwig K (2007) Isoplot/Ex version 3.41b, a geochronological toolkit for Microsoft Excel. Berkeley
889 Geochronology Center Spec. Publ. No 4:
- 890 Ludwig KR, Grauch RI, Nutt CJ, et al (1987) Age of uranium mineralization at the Jabiluka and Ranger
891 deposits, Northern Territory, Australia; new U-Pb isotope evidence. *Economic Geology* 82:857–874.
892 <https://doi.org/10.2113/gsecongeo.82.4.857>
- 893 Luo J-C, Hu R-Z, Fayek M, et al (2015) In-situ SIMS uraninite U–Pb dating and genesis of the Xianshi granite-
894 hosted uranium deposit, South China. *Ore Geology Reviews* 65:968–978
- 895 Maas R (1989) Nd-Sr Isotope Constraints on the Age and Origin of Unconformity-type Uranium Deposits in the
896 Alligator Rivers Uranium Field, Northern-Territory, Australia. *Economic Geology* 84:64–90.
897 <https://doi.org/10.2113/gsecongeo.84.1.64>
- 898 Martz P (2017) Caractéristiques, chronologie et rôles des circulations fluides dans le bassin d’Athabasca et son
899 socle: implications dans la formation et l’évolution du gisement d’uranium de Cigar Lake. PhD thesis;
900 Université de Lorraine
- 901 Martz P, Mercadier J, Perret J, et al (2019) Post-crystallization alteration of natural uraninites: Implications for
902 dating, tracing, and nuclear forensics. *Geochimica et Cosmochimica Acta* 249:138–159.
903 <https://doi.org/10.1016/j.gca.2019.01.025>
- 904 McKay AD, Mieziotis Y (2001) Australia’s uranium resources, geology and development of deposits. AGSO-
905 Geoscience Australia/ ISBN 0-642-46716-1
- 906 Mercadier J, Cuney M, Cathelineau M, Lacorde M (2011a) U redox fronts and kaolinisation in basement-hosted
907 unconformity-related U ores of the Athabasca Basin (Canada): late U remobilisation by meteoric fluids.
908 *Mineralium Deposita* 46:105–135. <https://doi.org/10.1007/s00126-010-0314-7>
- 909 Mercadier J, Cuney M, Lach P, et al (2011b) Origin of uranium deposits revealed by their rare earth element
910 signature. *Terra Nova* 23:264–269. <https://doi.org/10.1111/j.1365-3121.2011.01008.x>
- 911 Mernagh TP, Wygralak AS (2011) A fluid inclusion study of uranium and copper mineral systems in the
912 Murphy Inlier, Northern Australia. *Russ Geol Geophys* 52:1421–1435.
913 <https://doi.org/10.1016/j.rgg.2011.10.011>
- 914 Milidragovic D, Beaudoin G, Hamilton MA, King JJ (2016) The Paleoproterozoic Otish Gabbro suite and coeval
915 dyke swarms of the Superior Province: Probing the ca. 2.17 Ga mantle. *Precambrian Research* 278:126–
916 144
- 917 Murphy FC, Hutton LJ, Walshe JL, et al (2011) Mineral system analysis of the Mt Isa–McArthur River region,
918 Northern Australia. *Australian Journal of Earth Sciences* 58:849–873.
919 <https://doi.org/10.1080/08120099.2011.606333>
- 920 Page RW, Jackson MJ, Krassay AA (2000) Constraining sequence stratigraphy in north Australian basins:
921 SHRIMP U–Pb zircon geochronology between Mt Isa and McArthur River. *Australian Journal of Earth*
922 *Sciences* 47:431–459. <https://doi.org/10.1046/j.1440-0952.2000.00797.x>
- 923 Paton C, Hellstrom J, Paul B, et al (2011) Iolite: Freeware for the visualisation and processing of mass
924 spectrometric data. *Journal of Analytical Atomic Spectrometry* 26:2508–2518.
925 <https://doi.org/10.1039/C1JA10172B>

- 926 Plissart G, Féménias O, Mărunțiu M, et al (2009) Mineralogy and geothermometry of gabbro-derived listvenites
927 in the Tisovita–Iuti ophiolite, Southwestern Romania. *The Canadian Mineralogist* 47:81–105.
928 <https://doi.org/10.3749/canmin.47.1.81>
- 929 Polito PA, Kyser TK, Alexandre P, et al (2011) Advances in understanding the Kombolgie Subgroup and
930 unconformity-related uranium deposits in the Alligator Rivers Uranium Field and how to explore for
931 them using lithogeochemical principles. *Australian Journal of Earth Sciences* 58:453–474.
932 <https://doi.org/10.1080/08120099.2011.561873>
- 933 Polito PA, Kyser TK, Jackson MJ (2006) The role of sandstone diagenesis and aquifer evolution in the formation
934 of uranium and zinc-lead deposits, southern McArthur basin, Northern Territory, Australia. *Economic
935 Geology* 101:1189–1209. <https://doi.org/10.2113/gsecongeo.101.6.1189>
- 936 Polito PA, Kyser TK, Marlatt J, et al (2004) Significance of alteration assemblages for the origin and evolution
937 of the Proterozoic Nabarlek unconformity-related uranium deposit, Northern Territory, Australia.
938 *Economic Geology* 99:113–139. <https://doi.org/10.2113/gsecongeo.99.1.113>
- 939 Polito PA, Kyser TK, Rheinberger G, Southgate PN (2005a) A Paragenetic and Isotopic Study of the Proterozoic
940 Westmoreland Uranium Deposits, Southern McArthur Basin, Northern Territory, Australia. *Economic
941 Geology* 100:1243–1260. <https://doi.org/10.2113/100.6.1243>
- 942 Polito PA, Kyser TK, Thomas D, et al (2005b) Re-evaluation of the petrogenesis of the Proterozoic Jabiluka
943 unconformity-related uranium deposit, Northern Territory, Australia. *Mineralium Deposita* 40:257–288.
944 <https://doi.org/10.1007/s00126-005-0007-9>
- 945 Rawlings DJ (1999) Stratigraphic resolution of a multiphase intracratonic basin system: the McArthur Basin,
946 northern Australia. *Aust J Earth Sci* 46:703–723. <https://doi.org/10.1046/j.1440-0952.1999.00739.x>
- 947 Rheinberger GM, Hallenstein C, Stegman CL (1998) Westmoreland uranium deposits. *Geology of Australian
948 and Papua New Guinean mineral deposits: Melbourne, Australasian Institute of Mining and Metallurgy*
949 807–814
- 950 Richard A, Cathelineau M, Boiron M-C, et al (2016) Metal-rich fluid inclusions provide new insights into
951 unconformity-related U deposits (Athabasca Basin and Basement, Canada). *Mineralium Deposita*
952 51:249–270
- 953 Schindlmayr WE, Beerbaum B (1986) Structure related uranium mineralization in the Westmoreland district,
954 Northern Australia
- 955 Scott DL, Rawlings DJ, Page RW, et al (2000) Basement framework and geodynamic evolution of the
956 Palaeoproterozoic superbasins of north-central Australia: an integrated review of geochemical,
957 geochronological and geophysical data. *Australian Journal of Earth Sciences* 47:341–380.
958 <https://doi.org/10.1046/j.1440-0952.2000.00793.x>
- 959 Scrimgeour I, Kinny P, Close D, Edgoose C (2005) High-T granulites and polymetamorphism in the southern
960 Arunta Region, central Australia: Evidence for a 1.64Ga accretional event. *Precambrian Research*
961 142:1–27. <https://doi.org/10.1016/j.precamres.2005.08.005>
- 962 Shabaga BM, Fayek M, Quirt D, et al (2017) Mineralogy, geochronology, and genesis of the Andrew Lake
963 uranium deposit, Thelon Basin, Nunavut, Canada. *Can J Earth Sci* 54:850–868.
964 <https://doi.org/10.1139/cjes-2017-0024>
- 965 Sharpe R, Fayek M, Quirt D, Jefferson CW (2015) Geochronology and Genesis of the Bong Uranium Deposit,
966 Thelon Basin, Nunavut, Canada. *Economic Geology* 110:1759–1777.
967 <https://doi.org/10.2113/econgeo.110.7.1759>
- 968 Skirrow RG, Mercadier J, Armstrong R, et al (2016) The Ranger uranium deposit, northern Australia: Timing
969 constraints, regional and ore-related alteration, and genetic implications for unconformity-related
970 mineralisation. *Ore Geology Reviews* 76:463–503. <https://doi.org/10.1016/j.oregeorev.2015.09.001>

- 971 Stacey J, Kramers J (1975) Approximation of terrestrial lead isotope evolution by a two-stage model. *Earth and*
972 *planetary science letters* 26:207–221. [https://doi.org/10.1016/0012-821X\(75\)90088-6](https://doi.org/10.1016/0012-821X(75)90088-6)
- 973 Sun S-S, McDonough WF (1989) Chemical and isotopic systematics of oceanic basalts: implications for mantle
974 composition and processes. Geological Society, London, Special Publications 42:313–345
- 975 Tera F, Wasserburg GJ (1972) U-Th-Pb systematics in three Apollo 14 basalts and the problem of initial Pb in
976 lunar rocks. *Earth and Planetary Science Letters* 14:281–304. [https://doi.org/10.1016/0012-](https://doi.org/10.1016/0012-821X(72)90128-8)
977 [821X\(72\)90128-8](https://doi.org/10.1016/0012-821X(72)90128-8)
- 978 Vigar AJ, Jones DG (2009) Laramide Resources Limited. Westmoreland Uranium project. Redtree Resource
979 update/ Report MA823
- 980 Wall VJ (2006) Unconformity-related uranium systems: Downunder and over the top. *ASEG Extended Abstracts*
981 2006:1–12. <https://doi.org/10.1071/ASEG2006ab189>
- 982 Wilde AR, Mernagh TP, Bloom MS, Hoffmann CF (1989) Fluid inclusion evidence on the origin of some
983 Australian unconformity-related uranium deposits. *Economic Geology* 84:1627–1642.
984 <https://doi.org/10.2113/gsecongeo.84.6.1627>
- 985 Wilde AR, Wall VJ (1987) Geology of the Nabarlek uranium deposit, Northern Territory, Australia. *Economic*
986 *Geology* 82:1152–1168. <https://doi.org/10.2113/gsecongeo.82.5.1152>
- 987 Wingate MT, Pirajno F, Morris PA (2004) Warakurna large igneous province: A new Mesoproterozoic large
988 igneous province in west-central Australia. *Geology* 32:105–108. <https://doi.org/10.1130/G20171.1>
- 989 Wygralak AS, Ahmad M, Hallenstein CP (1988) Sedimentology of the Westmoreland Conglomerate, southern
990 McArthur basin, Northern Territory, Australia. *Journal of the Geological Society of Australia* 35:195–
991 207
- 992 Ypma PJM, Fuzikawa K (1980) Fluid inclusion isotope studies of the Nabarlek and Jabiluka uranium deposits,
993 Northern Territory, Australia. In: *Proceedings of International Uranium Symposium on the Pine Creek*
994 *Geosyncline*. IAEA, Vienna, pp 375–395
- 995 Zane A, Weiss Z (1998) A procedure for classifying rock-forming chlorites based on microprobe data.
996 *Rendiconti Lincei* 9:51–56. <https://doi.org/10.1007/BF02904455>
- 997 Zhou J-L, Li X-H, Tang G-Q, et al (2018) Ca. 890 Ma magmatism in the northwest Yangtze block, South China:
998 SIMS U-Pb dating, in-situ Hf-O isotopes, and tectonic implications. *Journal of Asian Earth Sciences*
999 151:101–111

1000

1001

1002 **Fig. 1** Schematic geological map of the study area, Northern Territory and Queensland, Australia. **a** Location of the
1003 McArthur and South Nicholson basins and Murphy Inlier in Australia. **b** Zoom indicating the location of the Alligator Rivers
1004 Uranium Field (ARUF) and the Westmoreland area (black rectangle). **c** Simplified geological map around the studied
1005 deposits of the Westmoreland area. After Ahmad et al. (2013).

1006

1007 **Fig. 2** Conceptual cross-section showing the position of the Junnagunna, Redtree, Huarabagoo and Long Pocket deposits in
1008 the stratigraphic sequence of the McArthur Basin, Australia (compilation after Fuchs and Schindlmayer 1981; Schindlmayer
1009 and Beerbaum 1986; International Atomic Energy Agency 2018a, b) and the approximate locations of the studied samples.

1010

1011 **Fig. 3** Paragenesis of the Redtree, Junnagunna and Huarabagoo deposits (Westmoreland area, Australia); compiled from
1012 Polito et al. (2005a) and this study. Ages are based on zircon U-Pb ages (Page et al. 2000) for the detrital minerals, U-Pb,
1013 $^{207}\text{Pb}/^{204}\text{Pb}$ and $^{40}\text{Ar}/^{39}\text{Ar}$ ages from Polito et al. (2005a) and U-Pb and Pb/Pb ages on apatite and uraninite from this study.
1014 *Italic*: data from the paragenesis presented by Polito et al. (2005a); *regular*: mineral sequence observed in this study; **bold**:
1015 mineral sequence observed in this study and by Polito et al. (2005a). The temperatures estimates are from chlorite and illite
1016 thermometry (Polito et al., 2005a; this study) and from the ΣREE (this study).

1017

1018 **Fig. 4** Photomicrographs and backscattered electron image (d) illustrating the diagenetic sequence for mineralized intercepts
1019 of the Redtree, Junnagunna and Huarabagoo U deposits (Westmoreland area, Australia). **a** Q0 detrital quartz grains coated by
1020 hematite (H1), and quartz overgrowths Q1, sample WDD10-151 27.9B. **b** Quartz partial dissolution (Q⁻) after Q1, sample
1021 JDD08-003 74.4A. **c** Rosette of chlorite C1 after partial dissolution of Q0 and Q1, sample WDD07-2 51.7A. **d** Diagenetic
1022 rutile R1 in a matrix formed by uraninite U4, sample WDD07-2 73.5B. **e** Illite alteration on chlorite C1, sample WDD9-128
1023 53.3B. **f** Quartz Q2 after quartz Q1, sample WDD07-2 55.9B.

1024

1025 **Fig. 5** Backscattered electron image images of uraninite mineral assemblages and location of the analyses from the Redtree,
1026 Junnagunna and Huarabagoo U deposits (Westmoreland area, Australia). For the location of the analyses: purple circle = LA-
1027 ICP-MS; blue cross = SIMS, dark green triangle = EPMA. **a** Uraninite U2 as matrix around apatite grains (Ap), sample
1028 JDD08-003 74.4B. **b** Uraninite U4 with altered zones, sample WDD07-2 55.9A. **c** Uraninite U4 in vein associated with
1029 chalcopyrite and pyrite, sample WDD10-151 29.4. **d** Uraninite U6 associated with clay minerals, sample WDD07-2 73.5B.

1030

1031 **Fig 6** EPMA maps of distribution of U, Pb, Ca, Fe and Si in uraninite for samples WDD07-2 55.9A (top) and WDD07-2
1032 73.5B (bottom, Westmoreland area, Australia). The U- and Pb-rich zones correlate with Ca- and Si-poor zones. The element
1033 concentration values (in wt%) are estimated from *in-situ* spot EPMA analyses.

1034

1035 **Fig. 7** Chemical compositions of uraninite generations from the Redtree, Junnagunna and Huarabagoo U deposits
1036 (Westmoreland area, Australia). **a** Pb vs Si + Ca + Fe. **b** Binary diagram of As vs Nb (in ppm). **c** Binary diagram of As vs W

1037 (in ppm). **d** Binary diagram of V vs Ba (in ppm). **e** Rare Earth Element abundance (ΣREE) vs. REE fractionation
1038 ($(\Sigma\text{LREE}/\Sigma\text{HREE})_N$) relative to published values from Mercadier et al. (2011b), Alexandre et al. (2016) and Martz et al.
1039 (2019). REE fractionation normalised to chondrite values of Anders and Grevesse (1989).

1040

1041 **Fig. 8** Chondrite-normalised REE patterns of the different uraninite generations from the Redtree, Junnagunna and
1042 Huarabagoo U deposits (Westmoreland area, Australia). Each generation exhibits a unique REE pattern indicating different
1043 chemical environments, as previously observed for the other minor and trace elements (Fig. 7). The C1 Chondrite
1044 normalization is after Sun and McDonough (1989). **a** U2 generation. Sample JDD08-003 74.4B. **b** U4 generation. The LREE
1045 enrichment indicated by the arrow corresponds to alteration indicated by Pb loss. The numbers indicated to the left of the
1046 diagram corresponds to the LA-ICP-MS spots presented in Fig. 5. Sample WDD07-2 55.9A. **c** U4 generation. Sample
1047 WDD10-151 29.4. **d** U5 generation. Sample WDD08-106 10.6. **e** U6 generation. Sample WDD07-2 73.5B. **f** Uraninite data
1048 from unconformity-related basement-hosted deposit in the ARUF (Mercadier et al. 2011b) and the Camie River deposit,
1049 Otish Basin, Canada (Lesbros-Piat-Desvial et al. 2017).

1050

1051 **Fig. 9** $^{238}\text{U}/^{206}\text{Pb}$ and $^{207}\text{Pb}/^{206}\text{Pb}$ ratios measured and related age on diagenetic apatite from the sample JDD08-003 74.4B
1052 (Junnagunna deposit, Westmoreland area, Australia). **a** Detrital quartz Q0 and diagenetic apatite in a uraninite U2 matrix
1053 (BSE image). **b** Tera–Wasserburg Concordia diagram.

1054

1055 **Fig. 10** U-Pb Concordia diagrams from in-situ isotopic analysis by SIMS of uranium oxides from the Redtree, Junnagunna
1056 and Huarabagoo U deposits (Westmoreland area, Australia). Plots were constructed using ISOPLOT (Ludwig 2007) from the
1057 isotope ratios presented in Table SM11. **a** Sample JDD08-003 74.4B. **b** The black ellipses are the data obtained on a single
1058 uraninite and the grey ellipses are additional data from the same depth in the same drillcore. Samples WDD07-2 55.9A and
1059 WDD07-2 55.9B. **c** Sample WDD10-151 29.4 anchored at 0 ± 5 Ma. **d** Sample WDD08-106 10.6 anchored at 0 ± 5 Ma. **e**
1060 Sample WDD07-2 73.5B anchored at 0 ± 5 Ma. **f** All data from this study (open circles, anchored at 0 ± 5 Ma) and from Polito
1061 et al. (2005a, pink).

1062

1063 **Fig. 11** Chlorite composition and nomenclature for the Redtree, Junnagunna and Huarabagoo U deposits (Westmoreland
1064 area, Australia). **a** Fe-Mg diagram indicating that all Fe atoms are in the Fe^{2+} state in the ferromagnesian chlorite. **b**
1065 Classification diagram after Plissart et al. (2009). **c** $\text{Al}^{\text{VI}}\text{-Al}^{\text{IV}}$ diagram for analysed chlorites. Structural formulae are
1066 calculated on the basis of 14 oxygen. **d** Classification diagram for rock-forming chlorites according to Zane and Weiss
1067 (1998). Compositions of chlorite from the Westmoreland area (this study; Polito et al., 2005a) are plotted together with

1068 chlorite from deposits of the ARUF (Polito et al. 2004, 2005b; Beaufort et al. 2005; Gigon et al. 2019), the Athabasca Basin
1069 (Kotzer and Kyser 1995; Billault et al. 2002; Martz 2017) and the Thelon Basin (Grare et al. 2020) for comparison. For data
1070 from the ARUF and the Canadian basins, the plotted data corresponds to the mean compositions for each sample or
1071 generation.

1072

1073 **Fig. 12** Synthesis of the alteration and mineralisation ages obtained in the ARUF and in the Westmoreland area of the
1074 McArthur Basin (Australia). 1: Hills and Richards (1976). 2: Clauer et al. (2015). 3: Ludwig et al. (1987). 4: Skirrow et al.
1075 (2016). 5: Polito et al. (2004b). 6: Polito et al. (2005b). 7: Maas (1989). 8: Polito et al. (2005a). 9: this study.

Figure 1

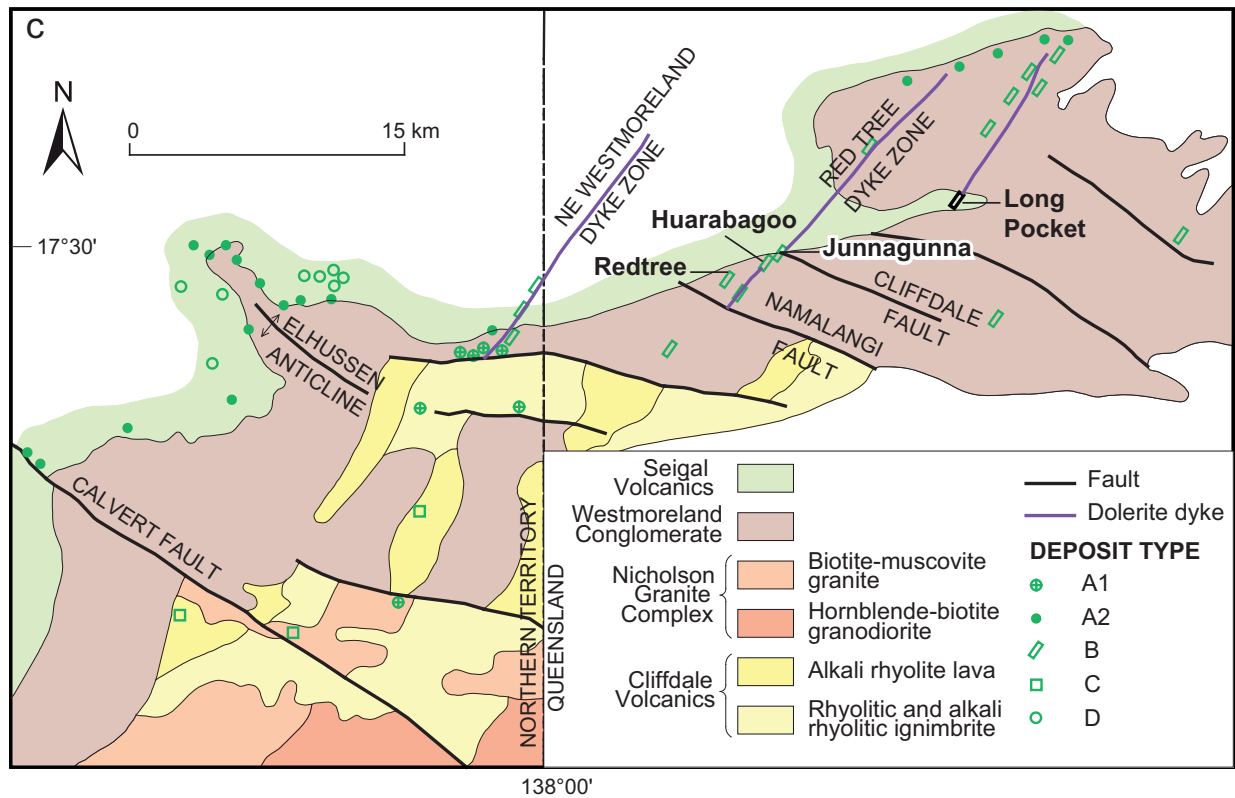
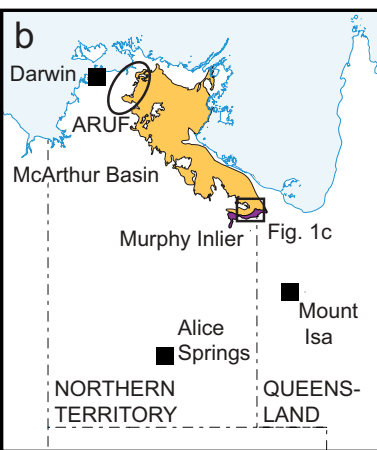
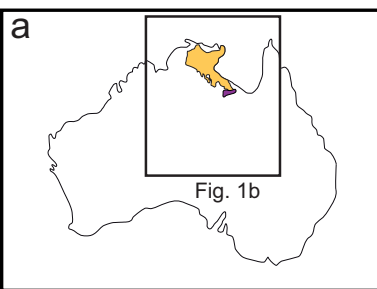


Figure 2

NW

SE

Junnagunna

Redtree

Huarabagoo

Long Pocket

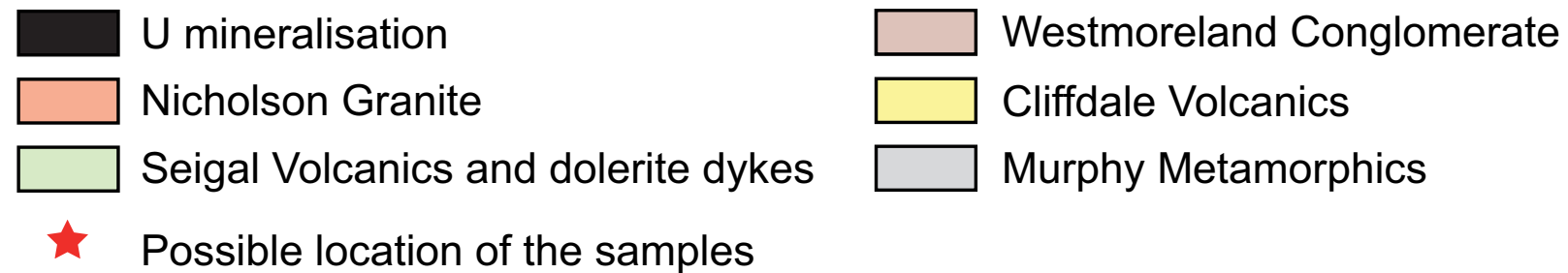
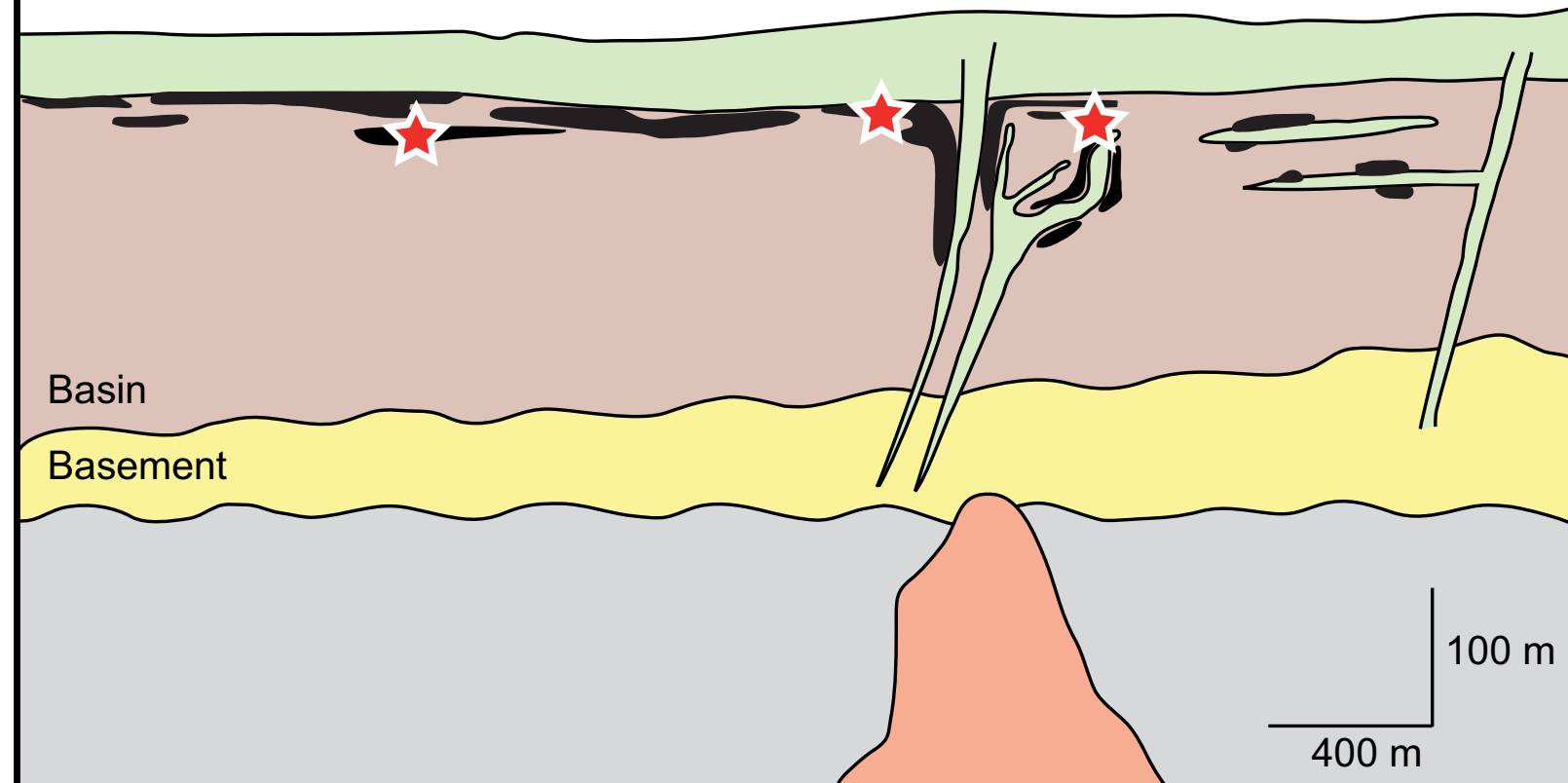


Figure 4

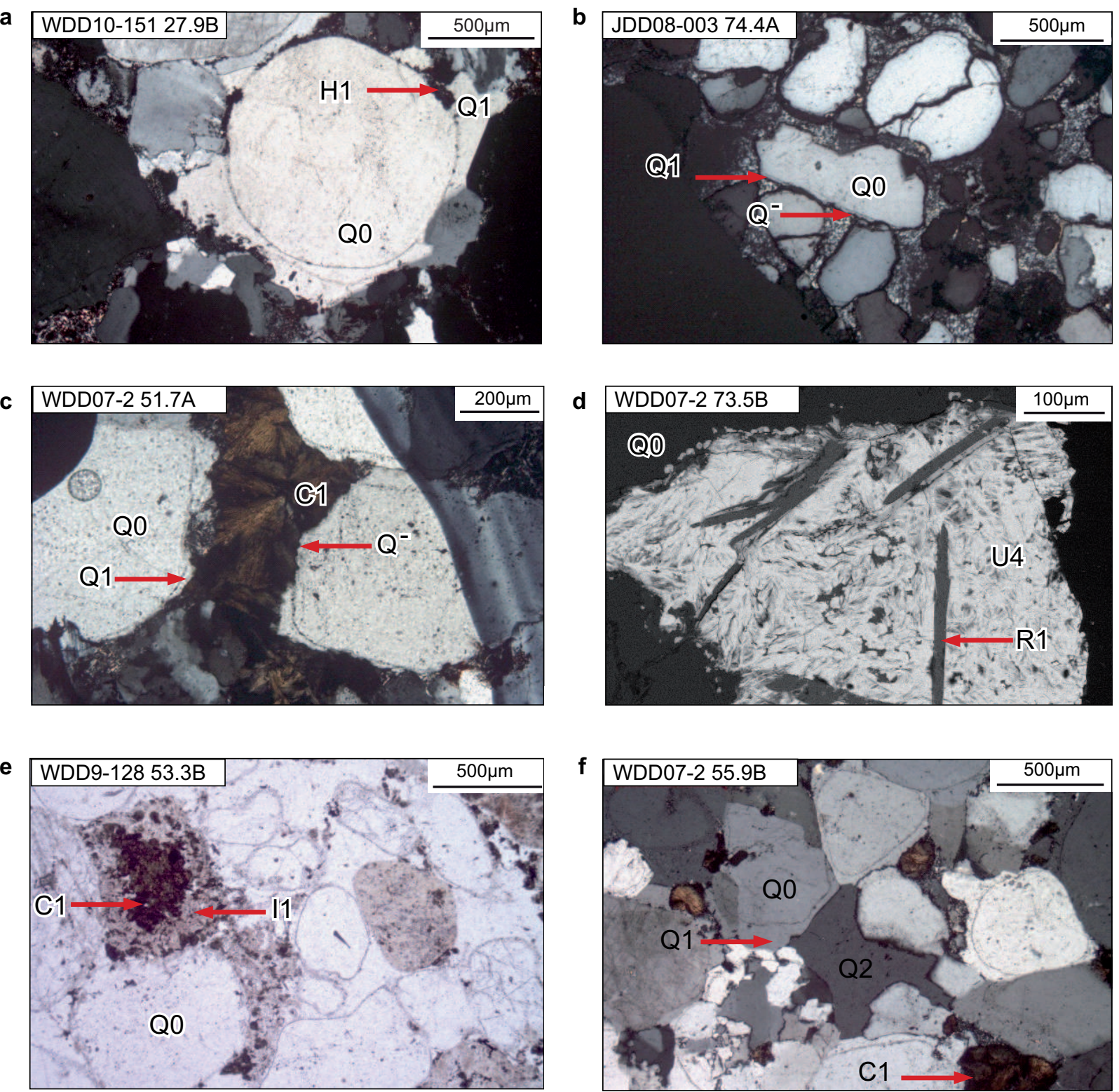


Figure 5

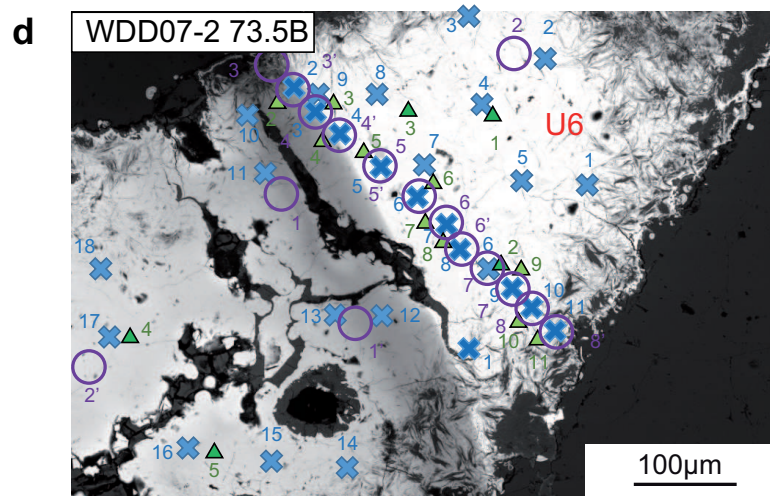
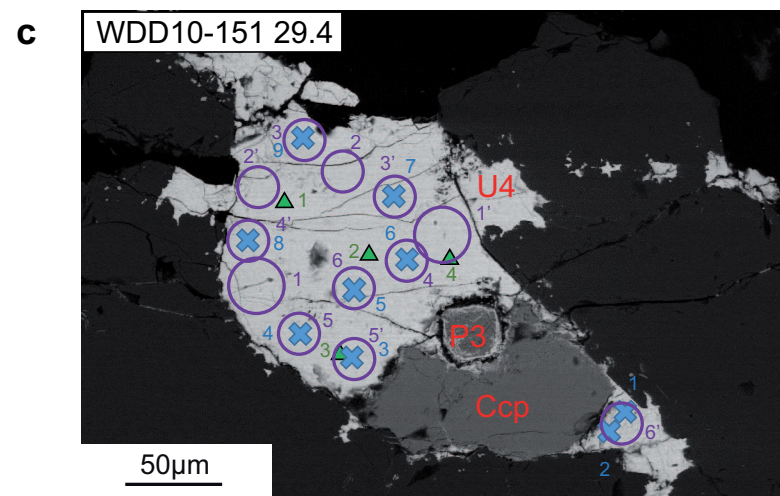
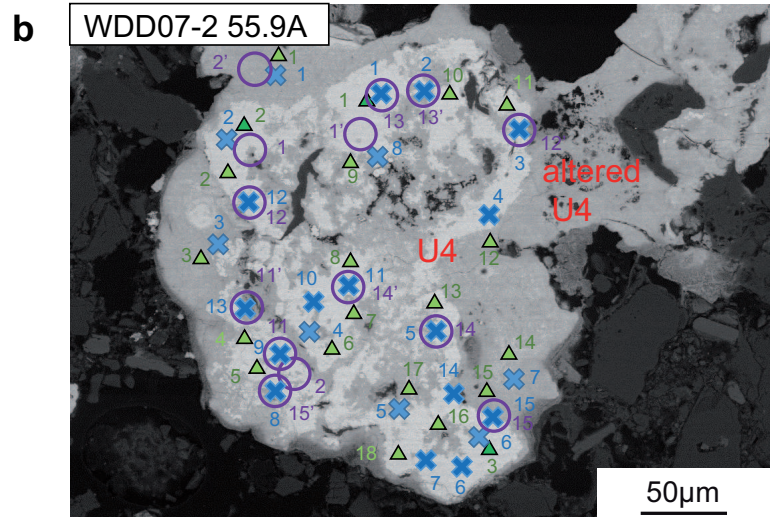
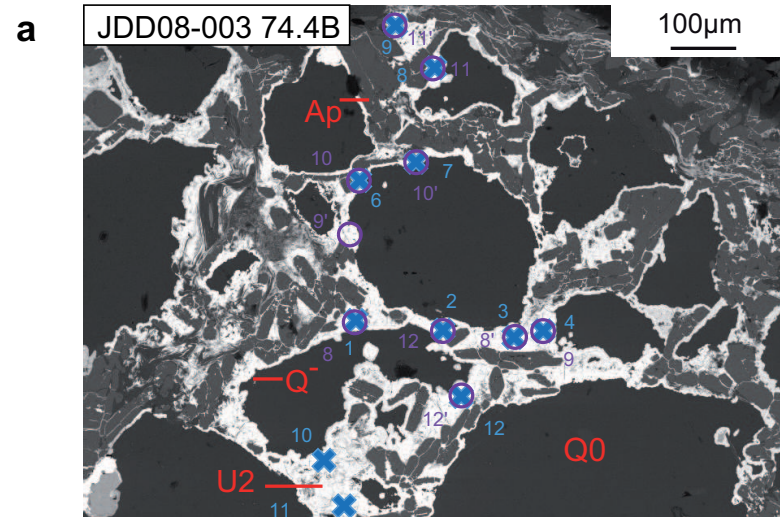
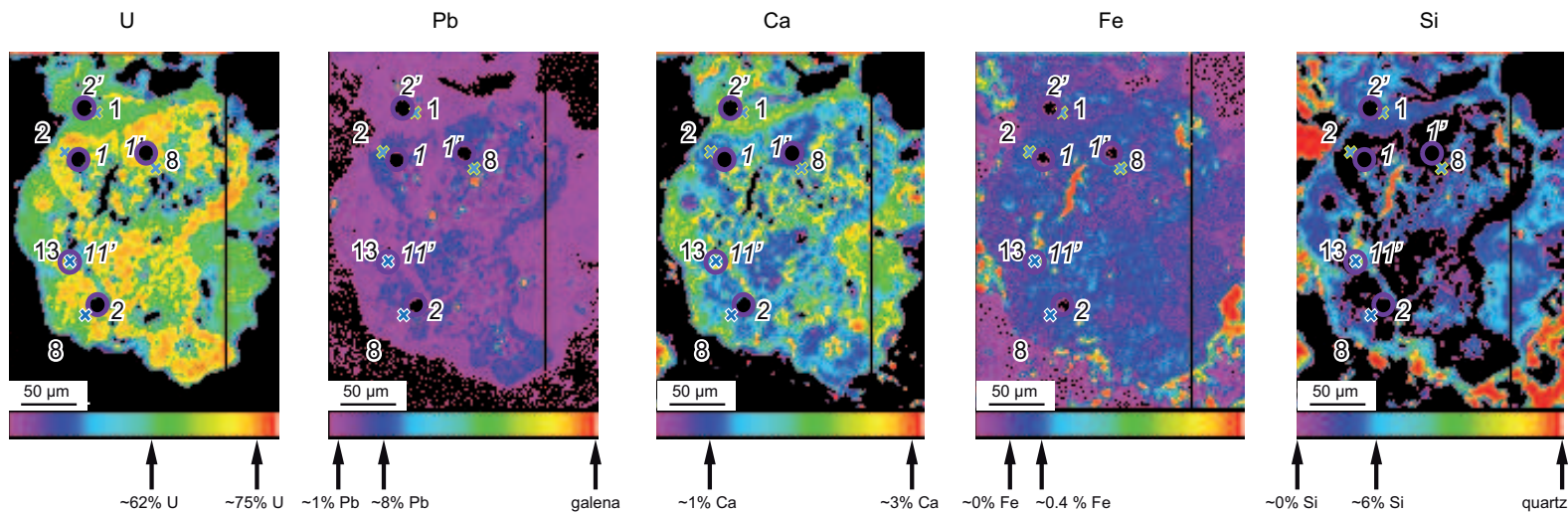


Figure 6

Sample WDD07-2 55.9A



Sample WDD07-2 73.5B

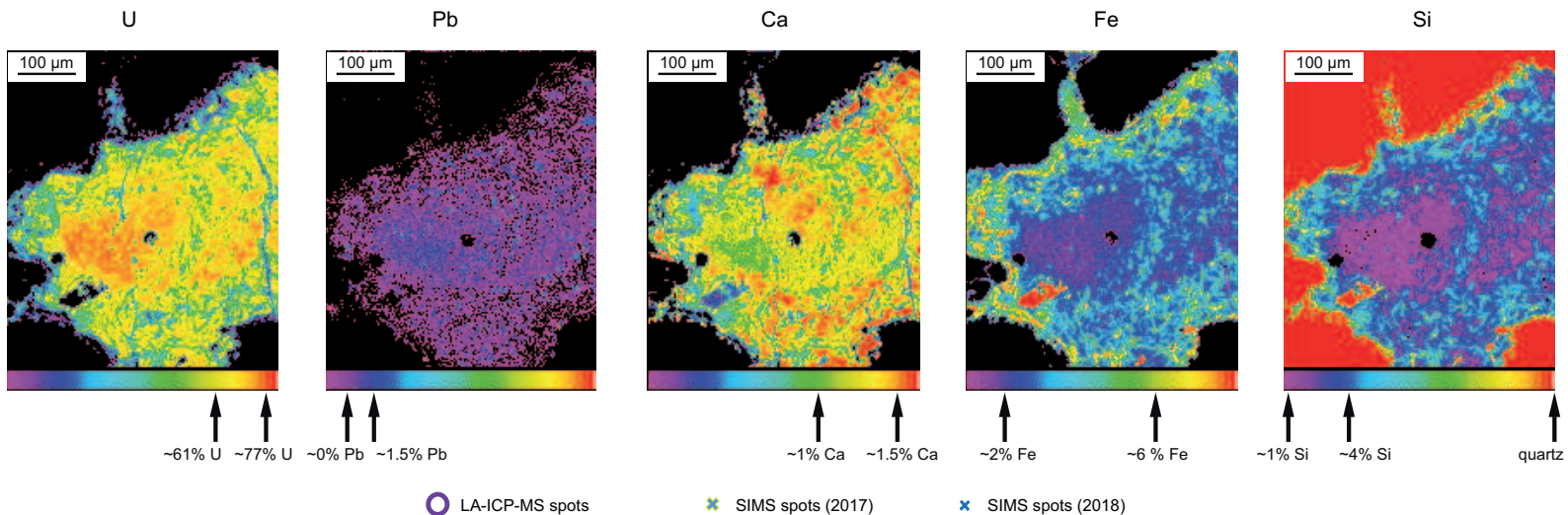


Figure 7

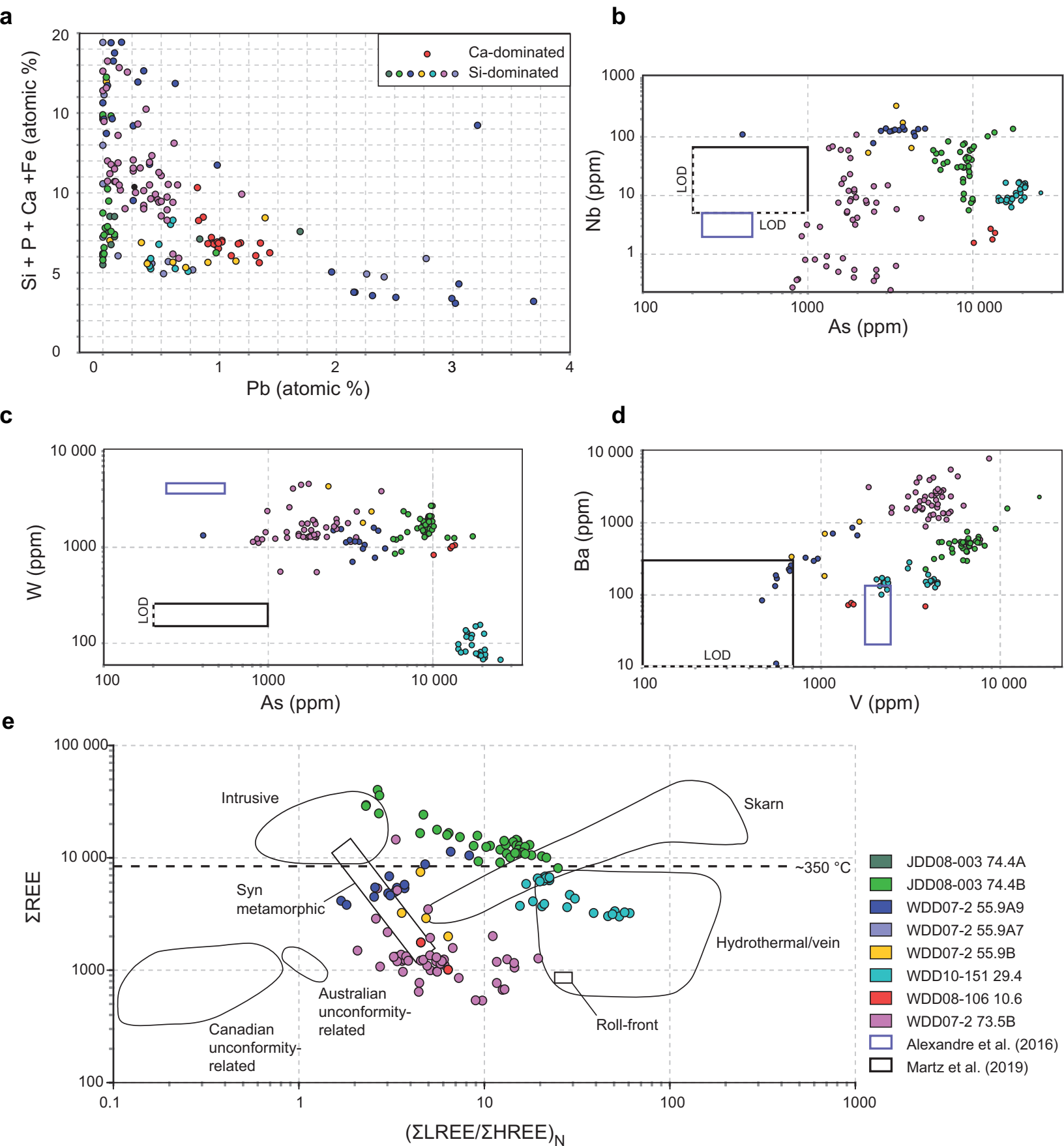


Figure 8

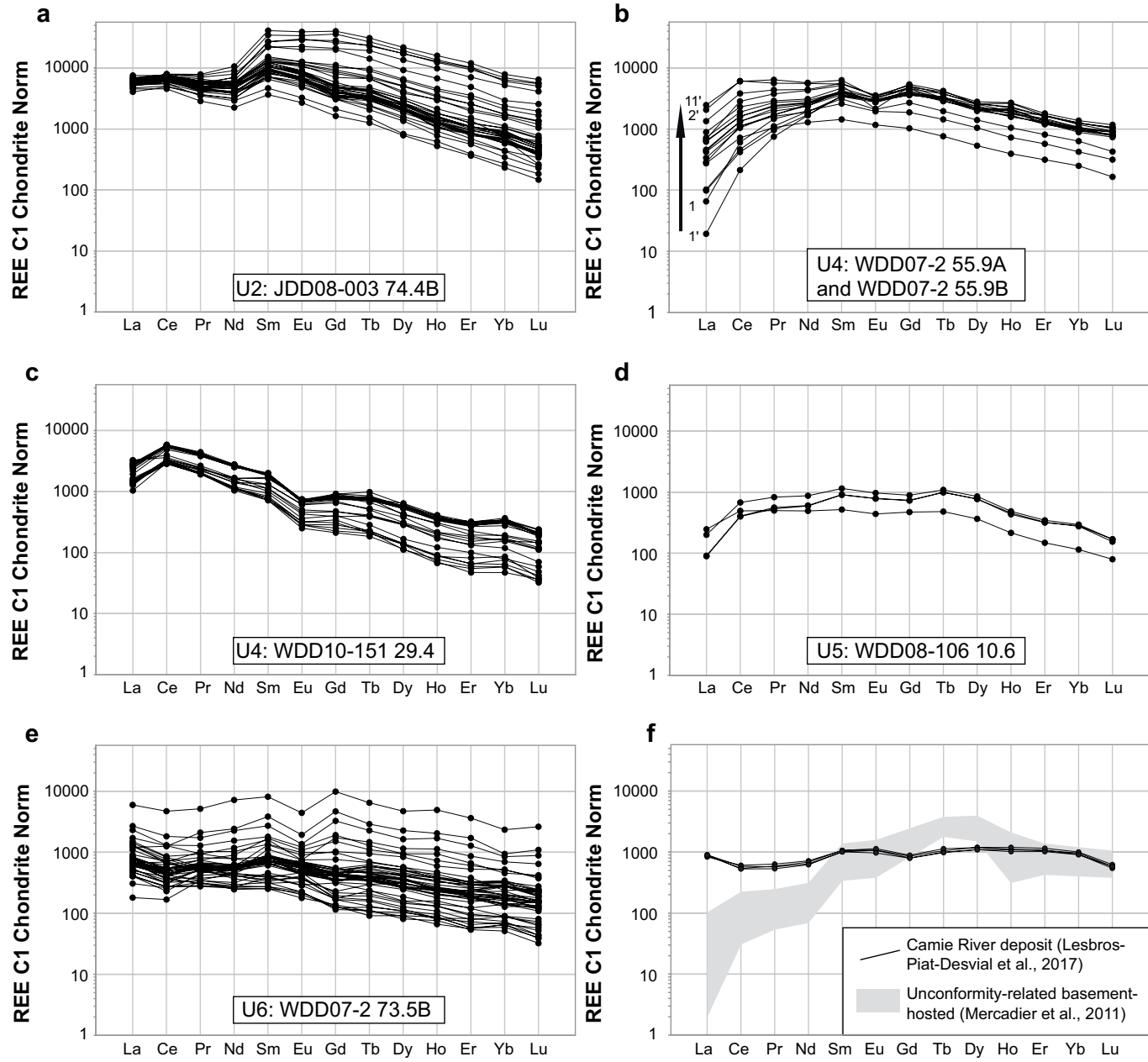


Figure 9

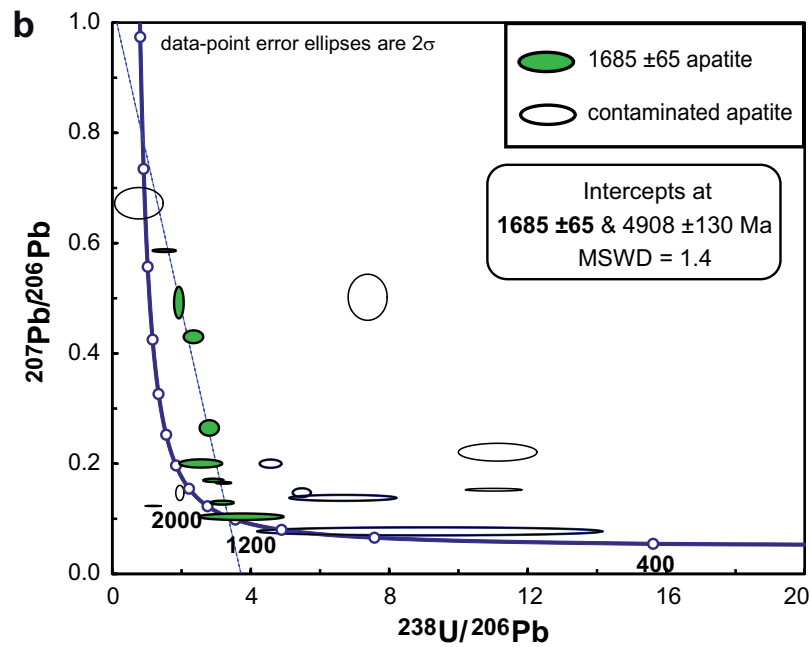
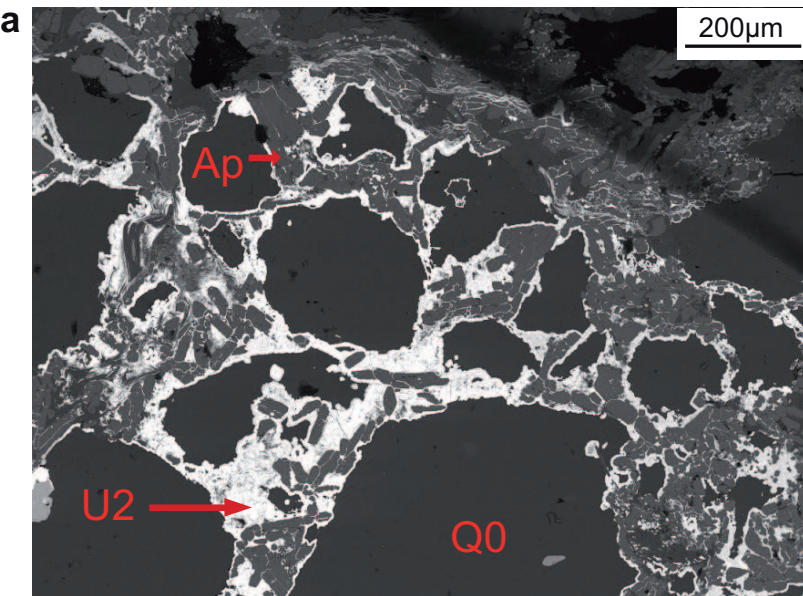


Figure 10

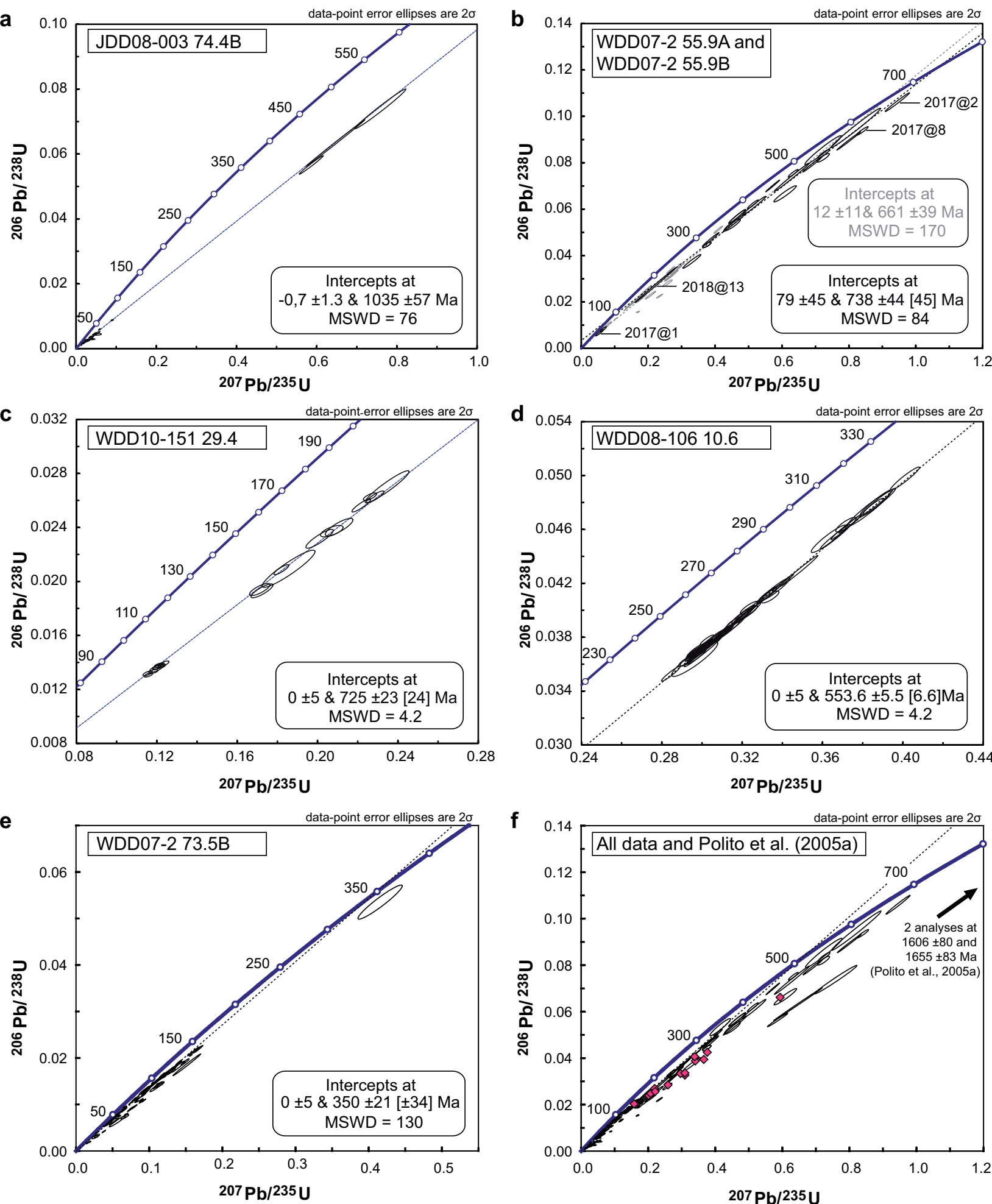
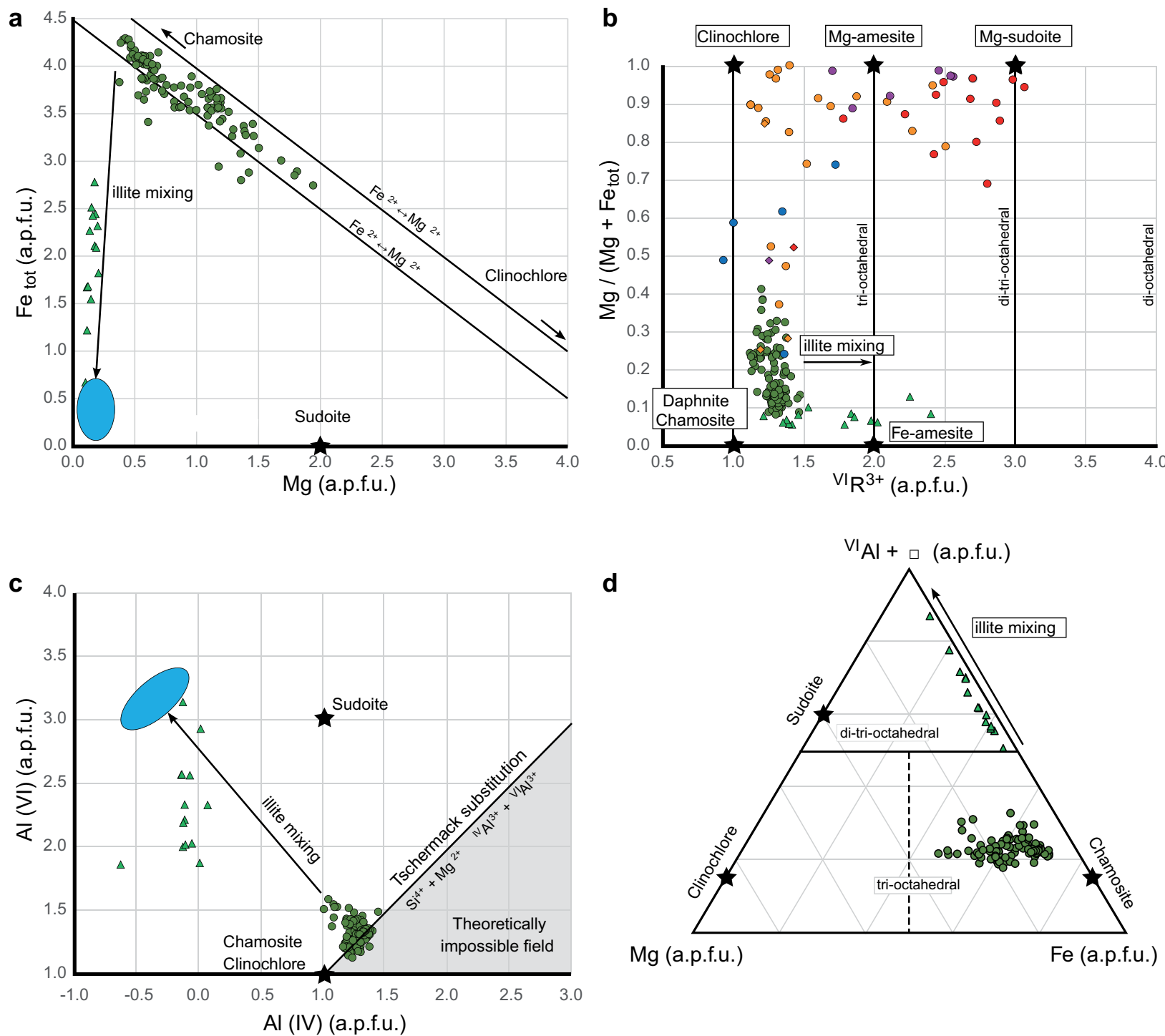
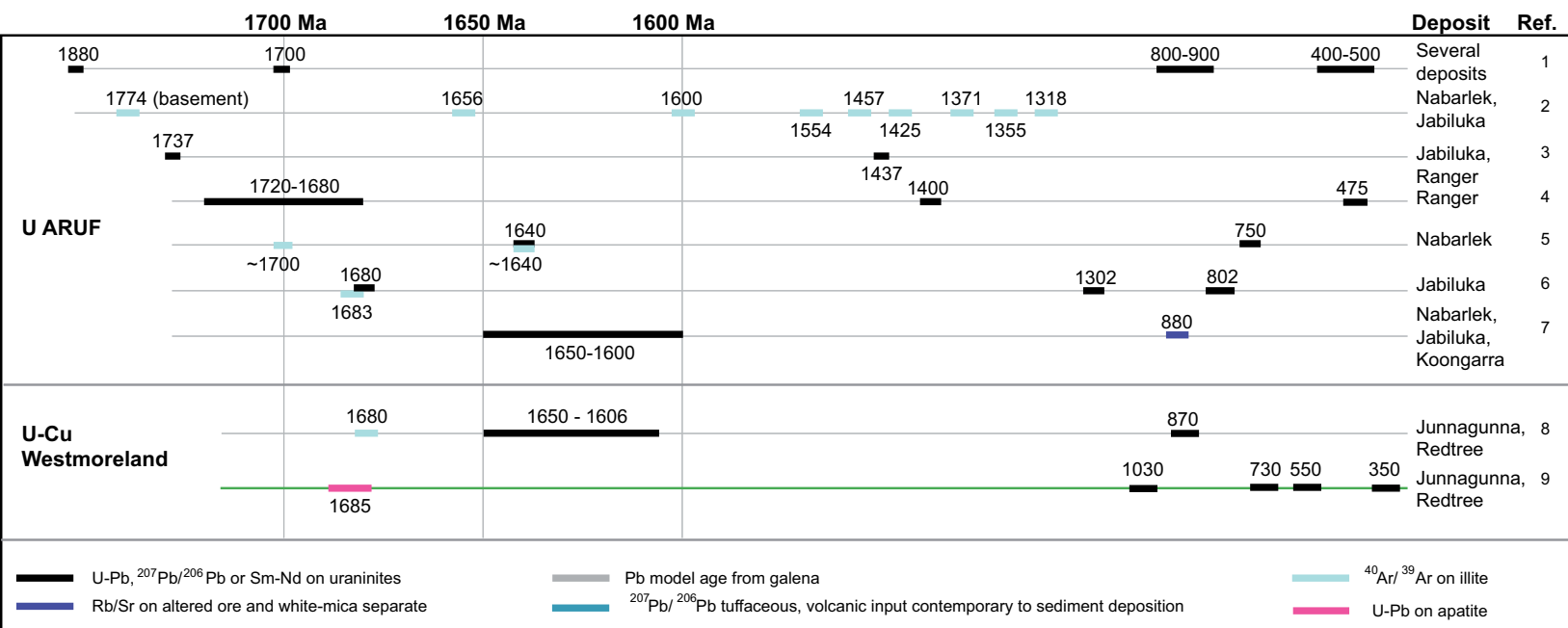


Figure 11



Westmoreland	ARUF	Athabasca Basin	Thelon Basin
● Chlorite	◆ Retrometamorphic chlorite	◆ Retrometamorphic chlorite	◆ Retrometamorphic chlorite
▲ Chlorite-illite mix	● Diagenetic/hydrothermal chlorite	● Diagenetic/hydrothermal chlorite	● Diagenetic/hydrothermal chlorite
● Illite			
● Chlorite C1 (Polito et al., 2005)			

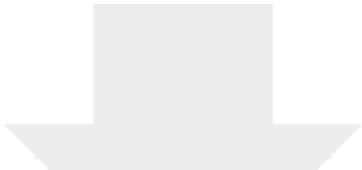
Figure 12





Click here to access/download
Supplementary Material
ESM1.pdf





Click here to access/download
Supplementary Material
ESM2.xlsx

